Global and Planetary Change 219 (2022) 103993

Contents lists available at ScienceDirect

Global and Planetary Change

journal homepage: www.elsevier.com/locate/gloplacha

A Eurasian Basin sedimentary record of glacial impact on the central Arctic Ocean during MIS 1–4

Linsen Dong [a,b], Leonid Polyak [c], Xiaotong Xiao [d], Stefanie Brachfeld [e], Yanguang Liu [a,b,*], Xuefa Shi [a,b,*], Xisheng Fang [a], Yazhi Bai [a], Aimei Zhu [a], Chaoxin Li [a], Song Zhao [a,f], Dong Wu [g], Chunjuan Wang [h]

[a] Key Laboratory of Marine Geology and Metallogeny, First Institute of Oceanography, Ministry of Natural Resources, Qingdao 266061, China
[b] Laboratory for Marine Geology, Pilot National Laboratory for Marine Science and Technology (Qingdao), Qingdao 266061, China
[c] Byrd Polar and Climate Research Center, Ohio State University, Columbus, OH, USA
[d] Frontiers Science Center for Deep Ocean Multispheres and Earth System, Key Laboratory of Marine Chemistry Theory and Technology, Ministry of Education,Ocean University of China,Qingdao 266100, China
[e] Department of Earth and Environmental Studies, Montclair State University, Montclair, NJ, USA
[f] School of Geographic and Oceanographic Sciences, Nanjing University, Nanjing, China
[g] College of Marine Geo-sciences, Ocean University of China, Qingdao, China
[h] Key Laboratory of Coastal Science and Integrated Management, Ministry of Natural Resources, Qingdao, Shandong Province 266061, China

ARTICLE INFO

Editor: Zhengtang Guo

Keywords:
Arctic Ocean
Eurasian Basin
Sediment stratigraphy
Radiocarbon dating
Magnetostratigraphy
Paleoceanography
Glacial history
Late Pleistocene

ABSTRACT

Pronounced Quaternary circulation and depositional changes in the Arctic Ocean basins remain poorly understood. We investigate sediment core ARC5-ICE4 (ICE4) in the Eurasian (Amundsen) Basin off the Lomonosov Ridge to reconstruct glacial-interglacial variability in sediment sources and circulation. The ICE4 record features variable lithologies including distinct glacigenic deposits with Ice Rafted Debris (IRD). The sediment age is constrained by a combination of the organic carbon ^{14}C with paleomagnetic data and correlation to earlier developed stratigraphies. The derived sedimentation rates constitute several cm/kyr (6.5 cm/kyr average) consistent with estimates from regional geophysical data. The developed age model covers the time interval from ca. 10 to 75 ka including Late and Middle Weichselian/Wisconsinian glaciations. Respective glacigenic sediments were primarily deposited by pulsed iceberg discharge. The Last Glacial Maximum and deglaciation is expressed in sharp IRD peaks including mineral proxies of the Laurentide Ice Sheet with an apparent millennial-scale variability. The older glacigenic sedimentary unit with abundant IRD of predominantly Siberian provenance was deposited during deglaciation of the Middle Weichselian (MIS 4/3) Eurasian Ice Sheet. These sedimentary differences indicate diverging impacts of the two glaciations on the Arctic Ocean, including ice-sheet sizes/geometries and oceanic circulation.

1. Introduction

The warming Arctic today suffers dramatic losses in the cryosphere including sea ice, glaciers, and permafrost (e.g., Peng et al., 2021; Slater et al., 2021; Tepes et al., 2021). Arctic sea ice alone accounts for almost 30% of the Earth's ice mass loss over the last ~25 years (Slater et al., 2021). This development induces major changes in physical, chemical, and biological processes in the Arctic Ocean (e.g., Polyakov et al., 2020; Steinbach et al., 2021; Wilson et al., 2021). Sedimentary records from the Arctic Ocean floor may hold clues to the history of many of these processes in the geological past. However, comprehension of these records is complicated by low and uneven sedimentation rates, scarcity of preserved paleobiological proxies, and limited hydrographic connection of the Arctic Ocean, especially during periods of low sea level. Furthermore, the history of glacigenic input from multiple circum-Arctic glaciations has considerable temporal and spatial heterogeneity that cannot be resolved without adequate age control and provenance identification.

* Corresponding authors at: Key Laboratory of Marine Geology and Metallogeny, First Institute of Oceanography, Ministry of Natural Resources, Qingdao, China.
E-mail addresses: dongls@fio.org.cn (L. Dong), polyak.1@osu.edu (L. Polyak), xtxiao@ouc.edu.cn (X. Xiao), brachfelds@mail.montclair.edu (S. Brachfeld), yanguangliu@fio.org.cn (Y. Liu), xfshi@fio.org.cn (X. Shi), fangxs@fio.org.cn (X. Fang), baiyazhi@fio.org.cn (Y. Bai), zhuaimei@fio.org.cn (A. Zhu), lichaoxin@fio.org.cn (C. Li), zhaosong@fio.org.cn (S. Zhao), wudong@fio.org.cn (D. Wu), cjw@fio.org.cn (C. Wang).

https://doi.org/10.1016/j.gloplacha.2022.103993
Received 26 January 2022; Received in revised form 2 November 2022; Accepted 7 November 2022
Available online 11 November 2022

In this study we test new, multi-proxy approaches to stratigraphy and depositional history of the central Arctic Ocean based on sediment core ARC5-ICE4 (ICE4) from a site in the Eurasian (Amundsen) Basin adjacent to the Lomonosov Ridge (LR) (Fig. 1). The LR is a major regional geological structure that traverses the Arctic Ocean from the Siberian to Greenland margin and plays an important role in controlling the oceanic circulation and glacial development (Björk et al., 2007, 2018; Jakobsson et al., 2001, 2016). Therefore, the LR has been the target of multiple geophysical and sediment coring operations (e.g., Spielhagen et al., 1997 Svendsen et al., 2004; Jakobsson et al., 2000, 2001, 2016; O'Regan et al., 2008 Jakobsson et al., 2014; Hanslik et al., 2010; Stein, 2019). In comparison, little is known about paleoceanographic history in the adjacent basins, where sedimentary records are complicated by downslope depositional processes and dissolution of biogenic sediment components (e.g., Backman et al., 2004; Svindland and Vorren, 2002; Pérez et al., 2020). Despite these challenges, information from sedimentary records in this area is needed for comprehending the central Arctic Ocean depositional setting and related paleoclimatic conditions, such as circulation and glaciation history.

In a prior study of core ICE4 focusing on paleomagnetic properties, Liu et al. (2019) observed a zone of negative inclination, which was interpreted as the Matuyama Chron. This interpretation results in very low estimated Quaternary sedimentation rates of ~1 mm/kyr, much lower than estimates from geophysical data indicative of an enhanced deposition in the Eurasian Arctic basins, including the Amundsen basin, during glacial intervals (e.g., Backman et al., 2004; Pérez et al., 2020; Weigelt et al., 2020). Our study tests the age model of Liu et al. (2019) and provides further insight through regional correlation of new ICE4 sedimentary proxy data supported by the ^{14}C dating of the organic carbon, leading to a reinterpretation of the paleomagnetic data. The results suggest that the ICE4 record contains variable lithologies in the age interval from ~10 to 75 ka, including distinct glacigenic (iceberg rafted) deposits that represent the last two major glaciations constrained to Marine Isotope Stages (MIS) 2 and 4/3. In addition to insights into depositional and related paleoclimatic environments in this climatically and oceanographically sensitive area, our results indicate sedimentation rates of several cm/kyr, consistent with geophysical data from the Amundsen Basin (e.g., Backman et al., 2004; Pérez et al., 2020; Weigelt et al., 2020). This substantial difference from an earlier estimate of Liu et al. (2019) highlights the need for a multi-proxy approach to evaluating sedimentary and paleoclimatic records in such a complex region as the Arctic Ocean.

2. Regional settings

The LR is a ~ 100–200-km-wide sliver of continental crust rifted

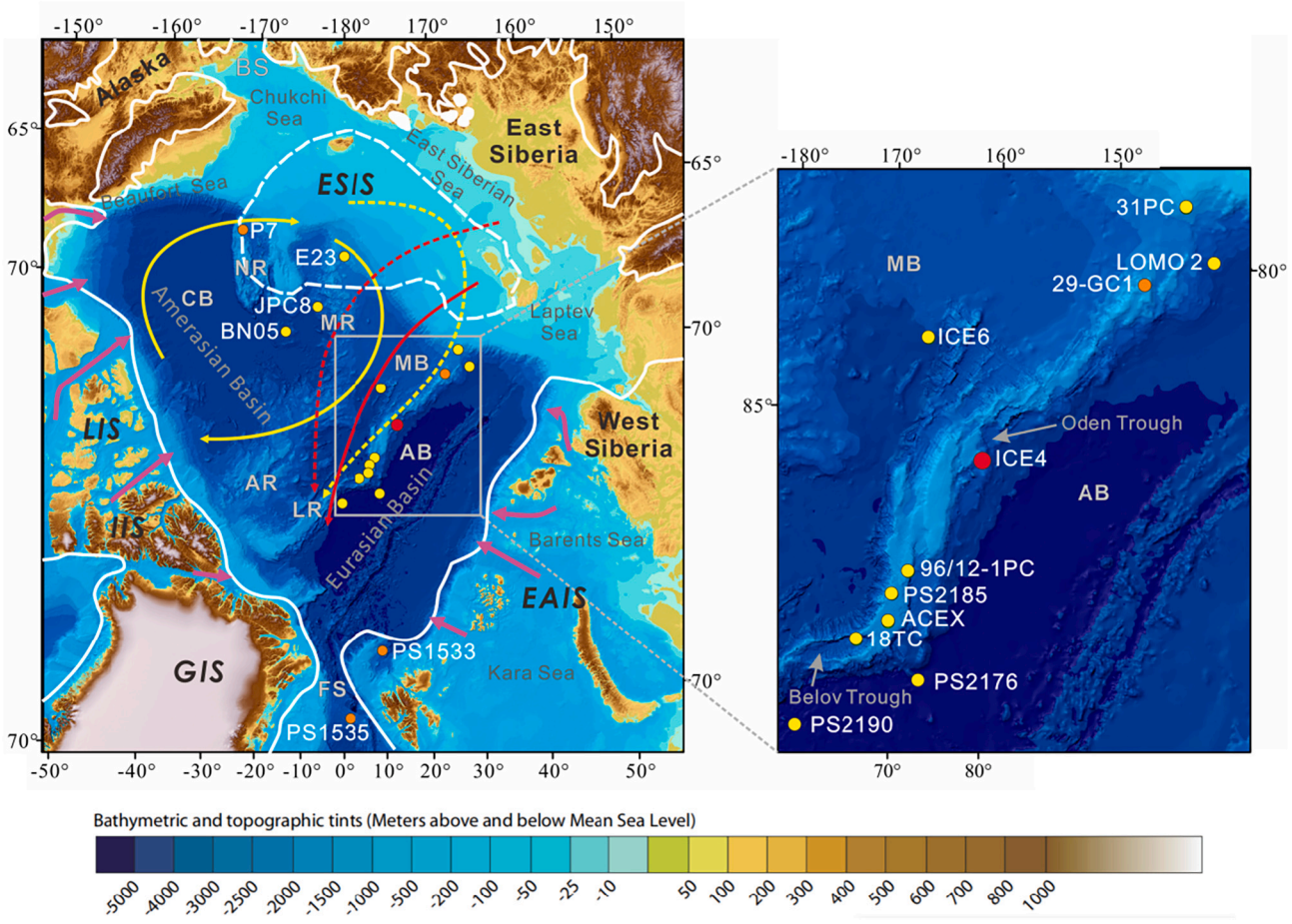

Fig. 1. Index map of the Arctic Ocean with location of ICE4 (red) and referenced sediment samples (orange - paleomagnetic data, yellow - other sites) (Supplementary Table S1). Lomonosov Ridge area (boxed) is shown in the inset. Major surface circulation systems, Transpolar Drift (TPD) and Beaufort Gyre (BG), are shown by red and yellow curved arrows, respectively. Solid and dashed arrow lines show climatological and extreme weak/strong-AO circulation modes (Volkov et al., 2020). White outlines indicate the inferred maximum extent of Pleistocene ice sheets around the Arctic Ocean (Batchelor et al., 2019): Laurentide (LIS), Innuitian (IIS), Greenland (GIS), Eurasian (EAIS), and Siberian (SIS, dashed outline for tentative limits). Purple arrows - major ice streams. LR, MR, AR, and NR - Lomonosov, Mendeleev, Alpha, and Northwind ridges; AB, MB, and CB - Amundsen, Makarov, and Canada Basins; BS, FS - Bering and Fram Straits. Base map is the International Bathymetric Chart of the Arctic Ocean (Jakobsson et al., 2012). (For interpretation of the references to color in this figure legend, the reader is referred to the web version of this article.)

from the Eurasian to Greenland margin in the early Cenozoic and translated northward to water depths close to 1 km sometime in the Miocene (e.g., Kristoffersen, 1990; Minakov and Podladchikov, 2012). The ridge constitutes a major barrier for the deep and intermediate water circulation, except for two narrow depressions (Oden and Belov troughs). During glaciations, the LR served as a critical pinning point for floating extensions of the circum-Arctic ice sheets that supported the inferred pan-Arctic ice shelf (Hughes et al., 1977; Polyak et al., 2001; Jakobsson et al., 2008; Jakobsson et al., 2014; Jakobsson et al., 2016; Gasson et al., 2018). Grounding of thick ice shelves and deep-keeled icebergs on the ridge top had a profound effect on sediment deposition on the slopes and in the adjacent basins (Polyak et al., 2001; Jakobsson et al., 2001, 2008, 2016; Kristoffersen et al., 2004; Pérez et al., 2020).

Sediment transport and deposition in the central Arctic Ocean is primarily controlled by two interacting surface circulation systems, the Transpolar Drift (TPD) and Beaufort Gyre (BG) (Fig. 1). Under modern conditions, the study area at the central LR is typically dominated by the TPD that exports sediment-laden ice from the Siberian shelves generally along the LR (Nürnberg et al., 1994; Pfirman et al., 1997). However, considerable shifts have been observed for the TPD-BG boundary depending on interannual to decadal, wind-controlled circulation changes known as the Arctic Oscillation (AO) (Rigor et al., 2002; Steele et al., 2004; Volkov et al., 2020). Strong/weak AO enhances the BG/TPD circulation resulting in strongly variable ice drift pattern (Fig. 1). On longer time scales, circulation may also have had a strong variability related to long-term glacial-interglacial changes in hydrographic and atmospheric conditions (Bischof and Darby, 1997; Dong et al., 2020; Wang et al., 2021; Xiao et al., 2021).

The ICE4 core site is proximal to the Oden Trough that breaches the LR approximately halfway between the North Pole and the Siberian margin, and serves as a conduit for intermediate water exchange between the Eurasian and Amerasian basins (Björk et al., 2018). This part of the LR displays glacial erosion and seepage mounds at the ridge top, sand waves on the slope, and potentially seismic events indicated by fractures in the ridge strata (Jakobsson et al., 2016; Pérez et al., 2020). Current activity may also be responsible for a local deepening at the slope base in front of the Oden Trough (Björk et al., 2018). All these features indicate a possibility of down- and off-slope sediment redeposition; however, no sizeable mass transport deposits (MTD) were found on the Eurasian side of the Oden Trough (Pérez et al., 2020).

Several studies addressed the depositional history and paleoenvironments of the central Arctic Ocean based on sediment cores from the central LR, primarily from its top (e.g., Spielhagen et al., 1997, 2004; Jakobsson et al., 2000, 2001; O'Regan et al., 2008; Jakobsson et al., 2014). These cores constitute widely used, stratigraphically constrained Arctic Ocean sedimentary archives including ACEX, a deep ocean drilling core that provides a long stratigraphic record (Backman et al., 2008; O'Regan et al., 2008). One of the major features in the upper part of this stratigraphy is a prominent increase in glacigenic sedimentation starting from MIS 6, ~190 ka (Fig. 2) (Jakobsson et al., 2001; Spielhagen et al., 2004; O'Regan et al., 2008; Jakobsson et al., 2014). Massive glacigenic deposits were related to major iceberg discharges from calving and collapsing marine ice sheets during glacial intervals and/or deglaciations. These sediments are characterized by a high content of coarse terrigenous grains and scarce to absent bio- and chemogenic

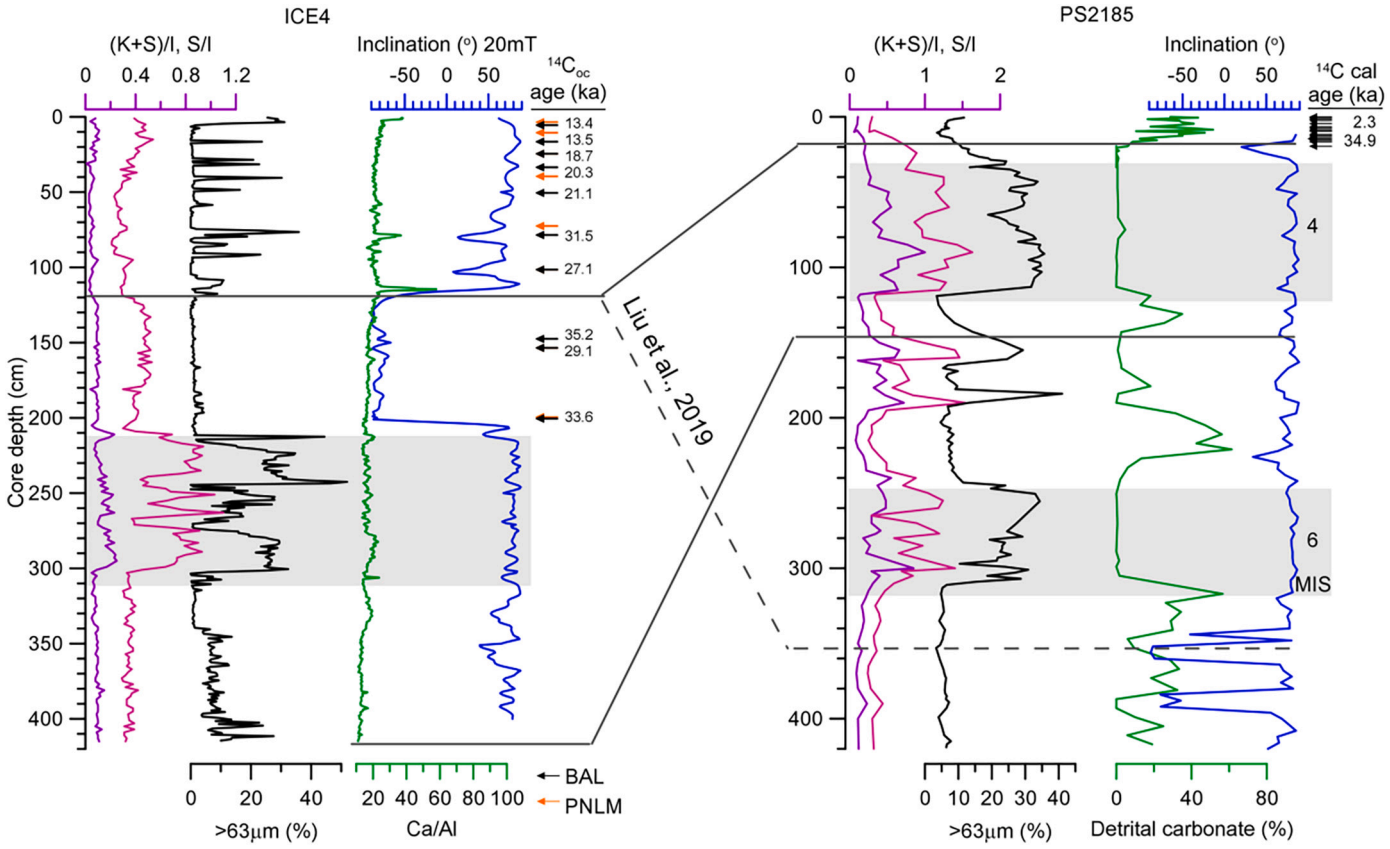

Fig. 2. Stratigraphic correlation of core ICE4 and PS2185 from the Lomonosov Ridge (Fig. 1; Spielhagen et al., 1997 Svendsen et al., 2004). Proxies shown include clay minerals smectite (S) and kaolinite (K) normalized to illite (I), coarse sediment content (>63 μm), paleomagnetic inclination, and detrital carbonate proxies (XRF Ca/Al for ICE4, detrital carbonate grains for PS2185). ^{14}C ages measured on TOC and foraminiferal tests are shown by arrows and numbers next to ICE4 and PS2185, respectively. Only the youngest ad oldest ^{14}C ages are numbered for PS2185 for presentation purposes. Arrows for ICE4 ^{14}C ages from the BAL and PNML are color-coded. Marine Isotope Stages (MIS) 4/3 and 6 are shown for major glacigenic units (highlighted in gray) next to PS2185. Correlation lines are shown based on this study (solid) and Liu et al. (2019) (dashed).

components. These features contrast with brownish, mostly fine-grained sediments representing interglacial/interstadial environments. The brown color in these layers is associated with high levels of manganese (Mn) delivered from continental shelves at higher sea levels and warmer climatic conditions (e.g., Jakobsson et al., 2000; März et al., 2011; Löwemark et al., 2012).

Consistently thick units of coarse ice-rafted debris (IRD) were related to glacigenic input during glacial/stadial intervals from MIS 6 to 3/4 (Fig. 2). In comparison, coarse sediment that would correspond to MIS 2 is not apparent in cores from the LR top, possibly due to strongly diminished sedimentation rates in the central Arctic Ocean during the Last Glacial Maximum (LGM) (Nørgaard-Pedersen et al., 2003; Polyak et al., 2009). A different pattern characterizes a well-dated core 18TC from deeper water in an intra-ridge depression (Belov Trough), where a hiatus occurs during the late MIS2 but sediments above and below have elevated IRD content (Fig. 1) (Hanslik et al., 2010). This difference between cores from the ridge top and the adjacent depression indicates a likelihood of sediment redistribution by currents and/or downslope processes. The location of core ICE4 at the foot of the LR slope provides a potential for a yet more complete characterization of MIS 2 sedimentation.

3. Material and methods

A 415-cm core ARC5-ICE4 was raised from 2860 mwd at 145°14.3′ E and 85°00′ N by the 5th Chinese Arctic Research Expedition (CHINARE-V) in 2012 (Ma, 2013) (Fig. 1). The split core was macroscopically described and logged for color reflectance and X-Ray Fluorescence (XRF) elemental composition. Samples for other analyses including grain size, mineralogy, and organic carbon were collected every 2 to 10 cm. Measurements were performed at the First Institute of Oceanography (FIO), Ministry of Natural Resources, China, unless indicated otherwise. As the core has no biogenic carbonate, the radiocarbon ages were determined by ^{14}C dating of the total organic carbon (TOC) in the upper 200 cm. We additionally re-evaluate the ICE4 paleomagnetic data from Liu et al. (2019) using a comparison to other published Arctic Ocean records and new data from core P1-92AR-P7 (P7) (Fig. 1). The resulting age framework was correlated to stratigraphic records from the LR (Spielhagen et al., 1997; Svendsen et al., 2004; Hanslik et al., 2010; Martens et al., 2020; Muschitiello et al., 2020), and more Arctic Ocean cores have been used for a broader paleoceanographic context (Fig. 1; Supplementary Table S1).

3.1. Non-destructive core scanning

Color reflectance was measured at 1-cm intervals using a hand-held Minolta CM-2002 spectrophotometer. Indices for lightness (L*) and red-blue channel (a*) were used to characterize the general sediment color. Relative elemental abundances were measured at 0.2-cm resolution using an Itrax XRF core scanner at 20 s count times, 10 kV X-ray voltage, and an X-ray current of 20 mA. In this study we use the distribution of manganese (Mn) and calcium (Ca) normalized to aluminum (Al), which are broadly used in the Arctic Ocean lithostratigraphy (e.g., Polyak et al., 2009; Löwemark et al., 2012; Schreck et al., 2018).

3.2. Grain size

For grain-size analysis, ~2-g sediment samples spaced at 1-cm intervals were successively treated with 15 mL 15% H_2O_2, 5 mL 3 M HCl, and 20 ml 1 M Na_2CO_3 for removing organic matter, biogenic carbonate and biogenic silica, respectively. Grain size measurements in the range of 0.02 to 2000 μm were performed on a Malvern Mastersizer 2000 laser particle analyzer. The relative error of repeated measurements was <3%. Sediments were classified according to Folk and Ward (1957). Grain size sorting was calculated for fine sediment (<63 μm) using the moment method (McManus, 1988).

3.3. Mineralogy

For bulk sediment mineralogy~5-g samples were taken at 2–5-cm and 10-cm spacing intervals above and below 130 cm, respectively. Sediment was dried, ground, passed through a 63-μm sieve, and loaded into aluminum holders. Samples were X-rayed from 5 to 65° 2θ with Cu K-alpha radiation (40 kV, 100 mA) using a step size of 0.02° 2θ and a counting time of 2 s per step on a D/max-2500 diffractometer (XRD) equipped with a graphite monochromator with 1° slits. Prior to the analysis, the instrument was blank corrected, and all samples were measured under the same conditions. Peak areas were estimated from XRD traces using Jade6.0 software, and semi-quantitative estimates of bulk mineral percentages were calculated following Cook et al. (1975). In addition to mineralogical analyses, >63-μm fraction from sandy samples was examined under the microscope for major petrographic components (Supplementary Table S2).

Samples for clay minerals determination (~5 g spaced at 2-cm intervals) were first treated with H_2O_2 (10%) and 1 M HCl to oxidize the organic matter and remove biogenic carbonates, respectively. Clay fractions (<2 μm) were obtained by the Atterberg settling tube method according to Stokes' Law. Each sample for the XRD analysis was transferred to two slides by wet smearing and air-drying. One slide was air dried at 60 °C for 2 h and analyzed. The second sample was solvated with ethylene glycol in a desiccator for at least 24 h at 60 °C. Every solvated sample was measured twice: the first scanning was done from 3° to 30° 2θ with a step size of 0.02°, and the second scanning from 24° to 26° 2θ with a 0.01° step. The latter was run as a slow scan to distinguish the 3.54/3.58 Å kaolinite/chlorite double peak. Proportions of clay mineral groups were calculated semi-quantitatively on ethylene glycol-saturated samples following Biscaye (1965), based on the peak areas of (001) series of basal reflections for smectite (including mixed layers, 15–17 Å), illite (10 Å), and kaolinite/chlorite (7 Å). Chlorite (004) and kaolinite (002) were identified at 3.54 Å and 3.58 Å, respectively.

Total silica content was measured at the same intervals with clay minerals using a combined gravimetric and photometric approach (e.g., Sun et al., 2019) at Shandong Provincial No. 4. Institute of Geological and Mineral Survey, China. Samples were mixed with sodium carbonate, leached with hydrochloric acid, and evaporated to a wet residue. Then, after the addition of hydrochloric acid and agglomerated silicic acid with animal glue, the mixture was filtered, heated and weighed. The residue was subsequently treated with hydrofluoric and sulfuric acids to remove silicon in the form of silicon tetrafluoride, and then calcined and weighed. The difference in mass before and after this treatment is the amount of silica in the precipitate. The final residue was melted with potassium pyrosulfate, extracted with water and incorporated into the silica filtrate. After depolymerization, the residual silica content in the filtrate was determined by the molybdenum blue photometry. The sum of the values from the two methods provided the total silica content with the relative standard deviation <5%.

3.4. Organic geochemistry

Organic geochemistry parameters include TOC and total nitrogen (TN), $\delta^{13}C_{org}$, and several biomarkers (n-alkanes, sterols, and glycerol dialkyl glycerol tetraethers (GDGT)). Highly branched alkane IP_{25} biosynthesized by sea-ice algae (e.g., Belt et al., 2007; Müller et al., 2009) was not detected, probably because the concentrations were below the instrument detection limit.

TOC and TN were measured at 2-cm intervals at FIO. Briefly, portions of the freeze-dried sediment samples (~1 g) were decalcified using 2 M hydrochloric acid, and the carbonate-free samples were then analyzed in duplicate using a Vario EL–III Elemental Analyzer with a standard deviation of 0.02 wt% ($n = 6$).

OC stable isotopes ($\delta^{13}C_{org}$), and biomarkers were analyzed at sparser intervals (10-cm average to 250 cm core depth, sparser below) in the

Key Laboratory of Marine Chemistry Theory and Technology, Ministry of Education, Ocean University of China. $\delta^{13}C_{org}$ was determined on carbonate-free sediments, pretreated as described above, using an isotope ratio mass spectrometer Thermo Scientific Delta V Advantage. The standard deviation was less than ±0.2‰ (n = 6), determined by six runs of IAEA-600, an inter-laboratory comparison standard distributed by the International Atomic Energy Agency (IAEA), Vienna. $\delta^{13}C_{org}$ values are reported in the δ notation relative to international standard V-PDB (Vienna Pee Dee Belemnite) in units of parts per mil (‰) and calculated as follows:

$$\delta^{13}C_{org}\ (‰) = \left[R_{sample}/R_{standard} - 1\right] \times 1000$$

where R_{sample} and $R_{standard}$ are the isotopic $^{13}C/^{12}C$ ratios of the samples and standards, respectively.

Extraction and purification of biomarkers follow the procedure of Zhao et al. (2006). Approximately 5 g of freeze-dried sediment was treated with dichloromethane:methanol (DCM/MeOH) (3:1, *v*/v) using sonication, after adding internal standards C_{19} *n*-alkanol, *n*-$C_{24}D_{50}$ and C_{46} GDGT. The extracts were first hydrolyzed with KOH in MeOH (6%) for 12 h and then extracted with hexane. The extracts were subsequently separated into fractions using silica gel chromatography. The hydrocarbon fraction containing *n*-alkanes was eluted with 8 ml of hexane. The polar lipid fraction was eluted with 12 ml dichloromethane/methanol (95:5, v/v), and divided into two aliquots. The aliquot for sterol measurements was derivatized using *N*,*O*-bis(trimethylsilyl)trifluoroacetamide (BSTFA) at 70 °C for 1 h before the instrumental analysis. The other aliquot was filtered using a PTFE 0.45 μm filter for GDGTs measurement.

Quantifications of normal alkanes (*n*-alkanes) and sterols was performed on an Agilent 6890 N GC with a FID detector with a precision of within <2% (1 SD, *n* = 10), using a HP-1 capillary column (50 m × 0.32 mm i.d., 0.17 μm film thickness, J&W Scientific) and H_2 as the carrier gas at 1.3 ml/min. For *n*-alkanes, the oven was kept initially at 80 °C for 1 min and then programmed to 200 °C at 25 °C/min, followed by 4 °C/min to 250 °C, 1.7 °C/min to 300 °C for 5 min, and finally 5 °C/min to 310 °C holding for 5 min. For sterols, the oven was kept initially at 80 °C for 1 min and then programmed to 200 °C at 25 °C/min, followed by 4 °C/min to 250 °C, 1.7 °C/min to 300 °C for 12 min, and finally 5 °C/min to 320 °C holding for 5 min. The content of alkanes and sterols was calculated from the ratio of their GC peak integrations to those of the *n*-$C_{24}D_{50}$ and C_{19} *n*-alkanol internal standard, reported as ng/g of bulk dry weight sediment (Zhao et al., 2006).

The *n*-alkane odd carbon number preference index (CPI) and the average chain length (ACL), both OC maturity (thermal alteration) indices, were determined as.

$$CPI = 1/2 \times [(C_{25}+C_{27}+C_{29}+C_{31}+C_{33})/(C_{24}+C_{26}+C_{28}+C_{30}+C_{32}) + (C_{25}+C_{27}+C_{29}+C_{31}+C_{33})/(C_{26}+C_{28}+C_{30}+C_{32}+C_{34})]$$

and

$$ACL = (C_{25} \times C_{25+27} \times C_{27+29} \times C_{29+31} \times C_{31+33} \times C_{33})/(C_{25}+C_{27}+C_{29}+C_{31}+C_{33})\ \text{(Zhang et al., 2006)}.$$

GDGTs were analyzed with an Agilent 1200 High Performance Liquid Chromatograph coupled to a triple quadrupole mass spectrometer (Waters-Quattro Ultima Pt) equipped with an atmospheric pressure chemical ionization (APCI) probe. GDGTs were eluted at a flow rate of 0.2 ml/min with hexane/isopropanol for the first 5 min, then with a linear gradient up to 1.8% isopropanol in 45 min in normal phase with a Prevail Cyano column (150 × 2.1 mm, 3 μm).

The HPLC-MS instrument was operated under the conditions of nebulizer 60 psi, vaporizer 400 °C, cone gas flow (N_2) 90 L/h and desolvation gas flow 600 L/h, APCI source 95 °C, APCI probe 550 °C. Single ion monitoring (SIM) was used because of its increased reproducibility and lower signal/noise ratio (Schouten et al., 2007). SIM was set to scan [M + H] + of crenarchaeol (GDGT-V; *m/z* 1292) and branched GDGTs Ia + IIa + IIIa (m/z 1050, 1036 and 1022), with a dwell time of 100 ms each. The relative abundances of GDGTs were obtained by comparing each respective [M + H] + peak area with that of the internal standard (m/z 744) (Huguet et al., 2006). The average relative standard deviation was <10%. The GDGT contents were calculated from the ratio of their peak integrations to those of the C_{46} GDGT internal standard, reported as ng/g of bulk dry weight sediment.

The Branched and Iisoprenoid Tetraether (BIT) index is based on the ratio of GDGT compounds and has been proposed for estimating the contribution of terrestrial organic matter transported from the soil (Hopmans et al., 2004):

BIT = (GDGT I+ GDGT II + GDGT III) / (GDGT I+ GDGT II + GDGT III+ Crenarchaeol), where GDGT I, GDGT II and GDGT III are branched GDGTs (brGDGTs).

3.5. Radiocarbon dating

No biogenic carbonate material was found in core ICE4, therefore ^{14}C dating was performed on bulk OC. Sixteen samples were analyzed for the AMS ^{14}C at the Beta Analytics Lab (BAL, US) and Pilot National Laboratory for Marine Science and Technology (PNLM, Qingdao, China) (Table 1). BAL procedure included $\delta^{13}C_{org}$ measured on-line with ^{14}C for fractionation correction. Ages were not calibrated due to the uncertainty with the OC sources as discussed below in Sections 4.5 and 5.3.1.

3.6. Paleomagnetic analyses

For a comparison with the ICE4 record generated by Liu et al. (2019), we present new paleomagnetic data from sediment record P1-92AR-P7/TC7 (combined piston and trigger core, hereafter referred to as P7) from the Northwind Ridge (Fig. 1). Lithostratigraphic context for this core was published earlier (Polyak et al., 2007). The core was sampled via U-channels, which were measured at the Laboratoire des Sciences du Climat et de l'Enviroment (LSCE) in Gif-sur-Yvette, France, on a 2G model 755-R cyrogenic magnetometer with in-line AF demagnetization unit. The natural remanent magnetization (NRM) was subjected to stepwise alternating field (AF) demagnetization, followed by acquisition and AF demagnetization of an anhysteretic remanent magnetization (ARM). ARM was acquired in a peak alternating field of 100 mT and a steady bias field of 0.05 mT at a translation speed of 1.0 cm/s. A relative paleointensity proxy was constructed from the average of the NRM/ARM ratio using the 20–40 mT alternating field demagnetization levels.

4. Results

4.1. General lithostratigraphy

Core ICE4 recovered a variety of lithologies that can be classified into seven major lithostratigraphic units based on the visual description and general lithological characteristics further refined by lithostratigraphic proxies (Fig. 3, Supplementary Fig. S1).

The scanned spectrophotometry data are consistent with the visual color characterization (Fig. 3, Supplementary Fig. S1). Darker-colored intervals are overall more brownish, as reflected in the lower L* and higher a* indices. Brown sediment has an overall slightly higher XRF Mn content, with the highest peaks corresponding to dark-brown laminae in Unit 4 and upper part of Unit 5, as well as near the core bottom. XRF Ca content is more consistent with lighter-colored gray intervals. The two highest Ca peaks occur in coarser sediment layers of Unit 2.

4.2. Grain size

The majority of ICE4 samples can be classified as silty mud, with a considerable amount of sand in Units 5 and 7, as well as isolated peaks in Units 1 and 2 (Fig. 3). Silt (2–63 μm) and clay (<2 μm) have an overall

Table 1
Radiocarbon dating results for sediment core ARC04-Ice4.

Depth (cm)	Lab ID	C age(years BP)	Error (years)	Δ14C (‰)	σ-Δ14C (‰)	IRMS $d^{13}C$	Material	Lab
3.5	QMLMA 190598	8290	70	−646.70	2.8		Bulk	PNLM
10.5	QMLMA 190599	10,340	80	−726.20	2.5		Bulk	PNLM
24.5	QMLMA 190600	12,920	80	−801.40	1.9		Bulk	PNLM
39.5	QMLMA 190601	15,960	70	−863.90	1.1		Bulk	PNLM
101.5	QNLMA 210020	23,100	180	−944.12	1.2		Bulk	PNLM
153.5	QNLMA 210021	29,430	340	−974.57	1.1		Bulk	PNLM
199.5	QNLMA 210022	35,890	740	−988.63	1.1		Bulk	PNLM
72.5	QNLMA 210019	30,570	390	−977.94	1.1		Bulk	PNLM
72.5	QNLMA 210245	29,070	270	−973.40	1.0		Bulk	PNLM
5.5	Beta-531,520	13,390	40	−812.74	0.94	−22.2	Bulk	BAL
16.5	Beta-571,208	13,520	30	−815.76	0.69	−22.2	Bulk	BAL
33.5	Beta-583,435	20,320	70	−920.99	0.69	−22.5	Bulk	BAL
50.5	Beta-571,209	21,080	70	−928.11	0.63	−22.9	Bulk	BAL
78.5	Beta-571,210	31,480	160	−980.30	0.4	−22.4	Bulk	BAL
101.5	Beta-571,211	27,140	120	−966.19	0.51	−23.6	Bulk	BAL
147.5	Beta-571,212	35,240	400	−987.67	0.62	−22.2	Bulk	BAL
200.5	Beta-582,955	33,600	220	−984.87	0.42	−22.8	Bulk	BAL
24–25	Beta-629,004	18,680	60	−902.26	0.73	−25.0	Bulk	BAL
153–154	Beta-629,005	29,130	160	−973.39	0.53	−22.4	Bulk	BAL

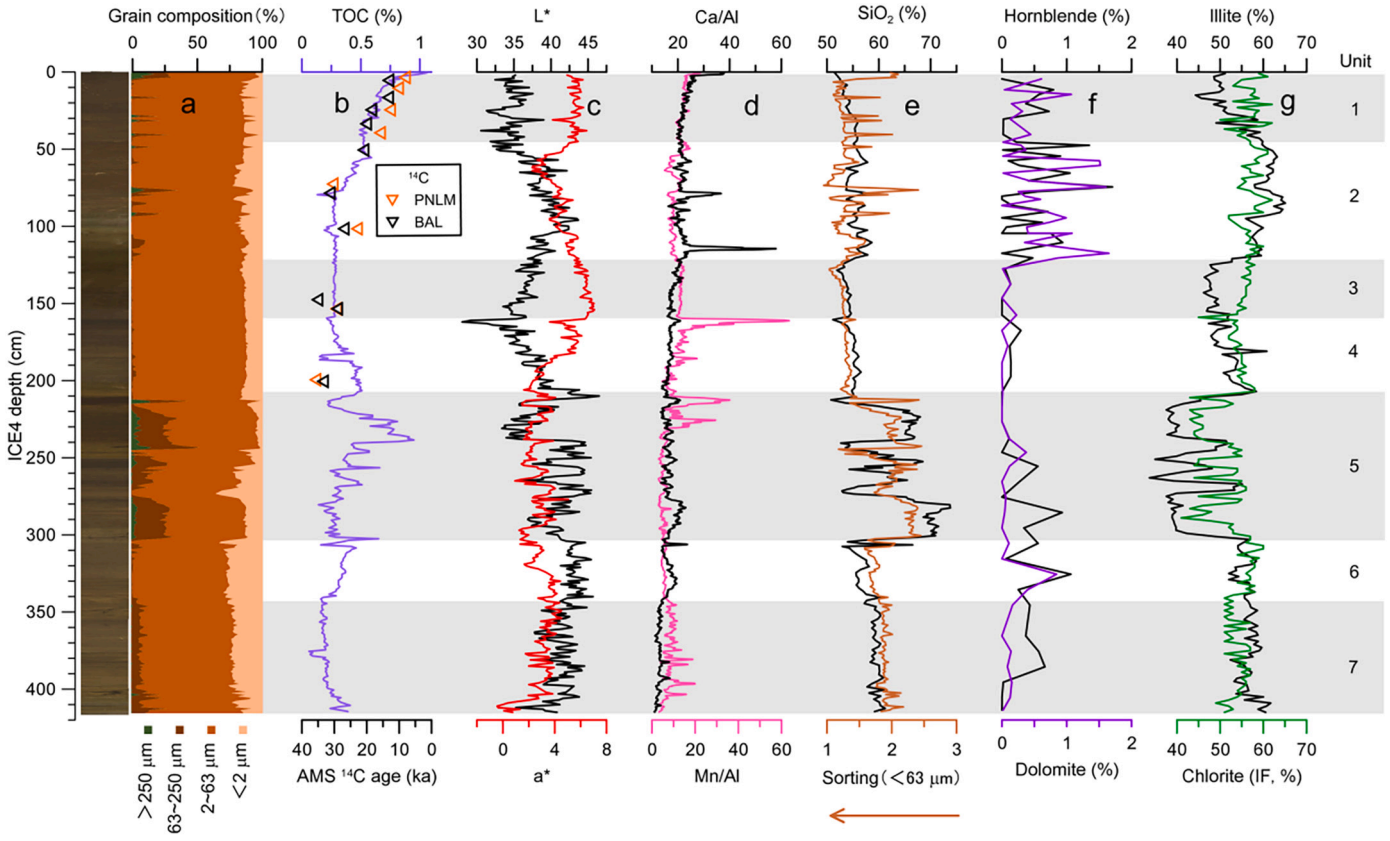

Fig. 3. Proxy records for core ICE4. (a) core photo and cumulative grain size; (b) TOC content and ^{14}Coc ages (symbols for PNML and BAL data are color-coded); (c) L* and a* color indices; (d)XRF Ca/Al and Mn/Al (5-pt average); (e) grain size sorting and silica content; (f) dolomite and hornblende content; (g) chlorite (illite-normalized) and illite clay mineral contents. Lithostratigraphic units 1–7 are highlighted and numbered. Photo width is stretched for readability.

distribution close to normal with 76% and 16% mean content, respectively. In comparison, the distribution of coarser grains is much more skewed as the content of sand (>63 μm) varies from 0 to 52% with 8% mean and 1% median values. Unit 5 has the highest occurrence of sand deposited mostly in broad bands 20–30-cm-wide each, where sand content ranges between ~10 and 50%. The coarsest grains (>250 μm) make up 18% of the assemblage in these intervals. Fine sediments (<63 μm) are generally well sorted in Units 1–4, except for sand peaks in Units 1 and 2, while sandy intervals of Units 5 are the least sorted.

4.3. Mineralogy

Clay minerals in ICE4 are predominated by illite (52% average), which is inversely related to chlorite, kaolinite, and smectite (26%, 17%, and 5% average, respectively). This inverse correlation, especially strong for chlorite and kaolinite ($R = -0.82$ and -0.89, respectively), indicates that the illite content may mask variations in the other clay minerals. Therefore, we also calculate the abundance of clay minerals for an illite-free (IF) composition. The IF chlorite generally co-varies

with illite (Fig. 3) and inversely correlates with both kaolinite and smectite, which are mostly abundant in Unit 5.

Bulk minerals are dominated by mica, quartz, and feldspars. The potassium feldspar to plagioclase ratio reaches the highest values in Unit 5 and some samples in Unit 1. Dolomite and hornblende are abundant in Unit 2 and some intervals in Units 1 and 5–7 (Fig. 3). Evaluation of the petrographic composition of sediment in coarse peaks also shows elevated presence of detrital carbonates in Unit 2 (Supplementary Table S2).

Total silica values range between 50 and 60% in most of the core, with prominent peaks up to ~75% in Unit 5 (Fig. 3). These peaks mostly co-vary with the distribution of coarse sediment grains.

4.4. Organic matter

TOC content is as high as >1% at the core top and persistently decreases to values <0.3% reached in the middle of Unit 2 (Figs. 3–4). In the lower part of Unit 4 TOC content increases again and shows considerable fluctuations reaching a peak of nearly 1% in Unit 5. Further downcore TOC falls to very low levels in Unit 7, with a slight increase at the core bottom. Distribution of the OC/N index is mostly consistent with TOC except for relatively stable low values in the upper part of the core, and some diversions from the TOC pattern in Unit 5. Stable carbon isotope $\delta^{13}C_{org}$ values are mostly in the range of −24 and − 22 ‰, rising to as high as −17 ‰ in Unit 6. The downcore pattern of $\delta^{13}C_{org}$ values typically opposes that of the OC/N ratio, especially in the lower part of the core (Units 4–7).

Distribution of *n*-alkanes shows a prevalence of long-chain homologues $\sum C_{27}+ C_{29} + C_{31}$ ranging between 500 and 2000 ng/g (Fig. 4). OC maturation indices CPI and ACL both decrease downcore (higher maturation), but show somewhat different patterns. CPI drops considerably from the core top to the middle of Unit 2, and then again in Unit 5. ACL stays relatively stable throughout Units 1–4, but drops sharply towards Unit 5, exhibiting strong fluctuations in its upper part and overall low values below.

GDGTs are characterized by overall low concentrations with prevailing branched GDGT reaching up to 500 ng/g (Fig. 4). Accordingly, the BIT index is high, mostly >0.5, consistent with numbers reported for other central Arctic Ocean records (Yamamoto et al., 2008; Yamamoto and Polyak, 2009).

Concentrations of brassica- and dinosterols are generally very low, <100 ng/g. The highest numbers occur in the upper part of Unit 2 and in the middle of Unit 5 (Fig. 4).

4.5. Radiocarbon ages

Sixteen ^{14}C determinations performed on TOC have an overall regular distribution pattern of uncalibrated ^{14}C ages increasing from ~10 ka BP at the core top to ~35 ka BP in the lower part of unit 4, with a few inversions (Fig. 3; Table 1). On-line BAL $\delta^{13}C_{org}$ measurements range mostly between −22 and − 23 ‰ consistent with the background $\delta^{13}C_{org}$ data. In comparison with the BAL data, most of the PNML ages are younger, by an average of ~15% estimated from BAL-PNML duplicates in three samples and interpolation for the rest of the data. The reason for this offset remains to be determined. The PNML has recently started operating and would benefit from an interlaboratory calibration with

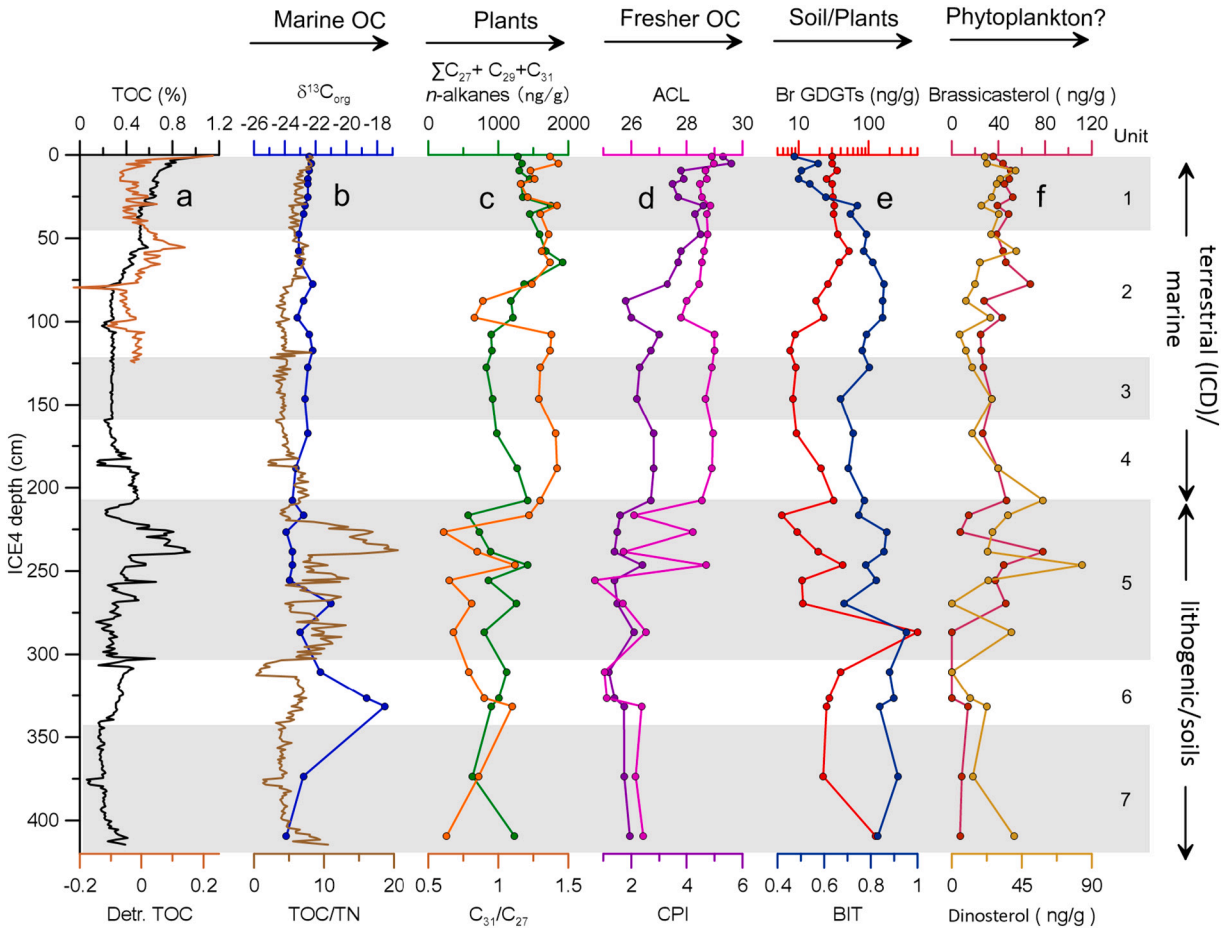

Fig. 4. Bulk organic matter and biomarkers in core ICE4. (a) TOC content (full core) and detrended TOC for the upper part; (b) $\delta^{13}C_{org}$ and OC/N ratio; (c) $\sum C_{27}+ C_{29} + C_{31}$ *n*-alkanes concentration and C_{31}/C_{27} ratio; (d) ACL and CPI maturation indices; (e) branched GDGT concentration and BIT index; (f) brassica- and dinosterols. Interpretation of the observed patterns is shown on the left and top. Lithostratigraphic units 1–7 are highlighted and numbered on top.

established laboratories such as the BAL.

4.6. Paleomagnetic data

Paleomagnetic results from ICE4 are reported in Liu et al. (2019). Sediments in core P7 used for a comparison carry a strong, stable remanence. A weak viscous component, possibly related to coring or to storage, is removed at the 10 to 20 mT demagnetization level. Inclination values are bimodal, with zones of steeply-positive and steeply negative inclination that fluctuate around the geocentric axial dipole (GAD) value of ±82°. The 20 to 50 mT AF demagnetization levels were used to define the characteristic remanence (ChRM). MAD values range from <1° to approximately 20°, with high MAD values generally due to noisy declination. As there is little power in the declination at this high latitude site, only inclination is used for this study. A relative paleointensity (RPI) proxy was constructed by normalizing the NRM with anhysteretic remanent magnetization (ARM) and calculating the average of the NRM/ARM curves using the 20 to 40 mT AF demagnetization levels.

5. Discussion

5.1. Sedimentary environments

5.1.1. Non-glacial sediments

The modern sedimentation in the central Arctic Ocean is dominated by settling from sea ice formed largely in the water column at the broad and shallow Siberian shelves (e.g., Nürnberg et al., 1994; Darby et al., 2009; Polyak et al., 2010). This sediment primarily originates from fine-grained material in suspension that is incorporated when ice forms in the fall. Some other types of ice, notably anchor ice formed at the sea floor, can incorporate coarser material, still dominated by grains not coarser than fine silt (Darby et al., 2009; O'Regan et al., 2014). Sea-ice controlled depositional environments resulting in mostly fine-grained sediments are inferred for interglacial/major interstadial intervals, when sea level was high and no ice sheets existed on the margins (e.g., Stein et al., 2012; O'Regan et al., 2014; Dong et al., 2017; Wang et al., 2021).

The fine-grained, relatively well-sorted sediment predominating ICE4, except for Units 5, 7 and coarse peaks in Units 1–2 (Figs. 3, 5), is comparable to sediment settling from sea ice. The typical fine-grained mode around ~4 μm occurs throughout ICE4 in various combinations with coarser fractions in Units 1–2, 5 and 7, and with finer grains in Units 3–4 (Fig. 5). This pattern is consistent with sediments with the mode at 2–4 μm interpreted as sea-ice entrainment and deposition (Darby et al., 2009; Dong et al., 2017; Wang et al., 2021). A relatively coarser overall composition of this sediment in units 1–2 may represent a combination of suspension freezing and anchor ice.

The inference of sea ice as a major depositional mechanism is consistent with a high content of illite and chlorite clay minerals in Units 1–4, which is indicative of transportation from the East Siberian continental margin in modern-type conditions (Wahsner et al., 1999; Viscosi-Shirley et al., 2003; Yamamoto et al., 2017; Ye et al., 2020). Chlorite content is especially elevated in Units 1 and 3, possibly indicating Chukchi Sea/Bering Strait provenance during periods of high sea levels (Yamamoto et al., 2017; Ye et al., 2020; Wang et al., 2021). The location of the ICE4 site in the pathway of the Transpolar Drift carrying sediment-laden ice from the East Siberian shelves (Fig. 1), is consistent with these provenance proxies. The exact provenance may have varied with changing drift patterns, such as the large swings related to the Arctic Oscillation (Rigor et al., 2002; Steele et al., 2004; Volkov et al., 2020).

In addition to sea ice, sediment from the continental margins can be transported into the central Arctic Ocean by lateral water flows. Data from sediment trap LOMO-2 at the Siberian LR end (Fig. 1) indicate about half of the terrigenous material transported laterally at water depths between 150 and 1550 m (Fahl and Nöthig, 2007). Nevertheless, provenance of this sediment is similar to sea-ice load. Sediment winnowing from sea floor affected by near-bottom currents can also contribute to deposition at larger water depths. Condensed stratigraphic records from the LR top are consistent with sediment winnowing and subsequent deposition on the slope or in local depressions (e.g., Fig. 2) (Spielhagen et al., 2004; Chiu et al., 2017).

Elevated background levels of sedimentary Mn, manifested also as high a* and low L* values (Fig. 3), are further indicative of interglacial-type conditions with material largely transported from the shelves (Jakobsson et al., 2000; O'Regan et al., 2008; Adler et al., 2009). We note however that XRF Mn content in ICE4 is overall lower than typical for interglacial intervals in Arctic Ocean cores, possibly due to the dilution by detrital material. Distinct Mn peaks in Unit 4 to the top of Unit 5, and in Unit 7 near the core bottom (Fig. 3) are likely indicative of fast Mn oxi (hydr)oxide precipitation in the oxidation fronts formed under pulsed fine-grained sediment deposition (Schoster, 2005; März et al., 2011). In the Arctic Ocean this type of sedimentation is typically observed stratigraphically above glacial intervals in cores from continental slopes and adjacent basins (Polyak et al., 1997; Wang et al., 2013). We infer a similar pulsed deposition for the upper part of Unit 5 to Unit 4, where fine sediment overlies distinct coarse-grained intervals composing the majority of Unit 5. The lower part of Unit 7, where Mn peaks occur between sandy layers, may represent similar conditions or, alternatively, sediment winnowing and resuspension up-slope from the core site.

5.1.2. Glacigenic sediments

In comparison with fine-grained interglacial sediment, glacial/

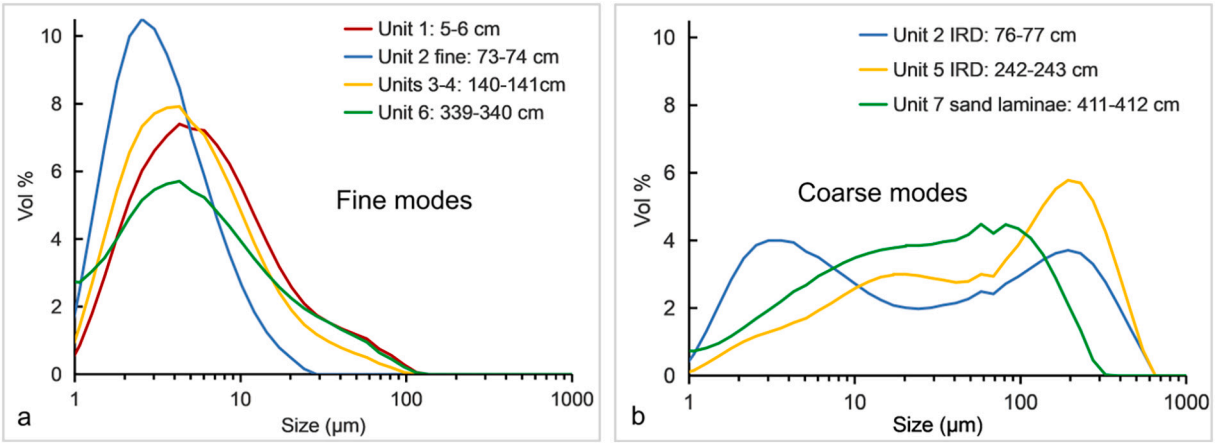

Fig. 5. Characteristic grain-size distribution patterns in ICE4 for predominantly fine and coarser sediment samples (left and right panels, respectively).

deglacial intervals in Arctic Ocean cores feature a distinct increase in coarse grains attributed to iceberg rafting (Stein et al., 2012; O'Regan et al., 2014; Dong et al., 2017). Icebergs carry entrained glacial material, which may have a wide grain-size distribution, but typically with a high content of coarse sediment (sand and larger) (Clark and Hanson, 1983; Andrews, 2000). Pronounced peaks of coarse IRD have been attributed to iceberg discharge events and tracked to Arctic Eurasian or North American ice-sheet margins (Bazhenova et al., 2017; Kaparulina et al., 2016; Dong et al., 2017, 2020; Wang et al., 2021). Distinct layers enriched in coarse IRD related primarily to Eurasian sources characterize glacial intervals in the LR cores starting with MIS6 (Fig. 2; Jakobsson et al., 2001; Spielhagen et al., 2004; O'Regan et al., 2008, 2014). In contrast, glacigenic deposits in cores from the western (Amerasian) Arctic Ocean typically have higher amount of North American IRD identified by detrital carbonates, mostly dolomites from the northwestern Laurentide Ice Sheet (LIS) sector (Bazhenova et al., 2017; Dong et al., 2017, 2020; Wang et al., 2021).

Unlike the rest of core ICE4, Unit 5 features poorly sorted sediment with coarse grains in various size fractions (e.g., >63 and 250 μm: Figs. 3, 5). This pattern is very similar to glacial IRD intervals in the LR cores, and closely resembles the interval attributed to the MIS4 glaciation (Fig. 2; Jakobsson et al., 2001; Spielhagen et al., 1997, 2004; O'Regan et al., 2008, 2014). The coarse IRD abundance in Unit 5 co-varies with the total silica content (Fig. 3), indicating a high contribution of quartz-rich rocks, which are common for Siberian sources (Vogt, 1997; Stein, 2008). The clay mineral assemblage in Unit 5 has elevated contents of smectite and kaolinite, as observed also in the correlative interval on the LR top (Fig. 2; Spielhagen et al., 1997). An increase in these minerals in association with coarse sediment in Arctic Ocean cores has been attributed to iceberg rafting of glacially eroded material (Vogt and Knies, 2009; Krylov et al., 2014: Dong et al., 2017; Ye et al., 2020). The likely source of smectite is igneous rocks of the western Siberia, where the Siberian Large Igneous Province (SLIP) was overridden by the Eurasian Ice Sheet (EAIS) (Vogt, 1997; Vogt and Knies, 2009). Elevated kaolinite content in glacial intervals has been related to the LIS provenance (Ye et al., 2020; Wang et al., 2021). More sources may have existed along the Arctic margins during non-analogous glacial conditions (Dong et al., 2017).

Glacigenic origin is also inferred for distinct, sharp coarse-grained peaks with a relatively regular occurrence in Units 1–2 (Figs. 2-3). These peaks have a grain size distribution that is similar to more massive IRD layers in Unit 5 (Fig. 5). The inference of glacigenic sources is consistent with the mineral and elemental composition of Units 1–2, which have the highest background level of bulk Ca in the core, with two pronounced peaks in the middle and lower part of Unit 2 (Figs. 2-3). Detrital carbonates are also abundant in Unit 2 (Supplementary Table S2), and the bulk minerals have elevated dolomite and hornblende content (Fig. 3). While the hornblende sources are not yet well understood, high detrital carbonate content is indicative of glacigenic input from the LIS (Bazhenova et al., 2017; Dong et al., 2017, 2020; Wang et al., 2021). While much of the correlative deposits in other LR cores may be missing due to the LGM hiatus, the adjacent sediments clearly show elevated content of detrital carbonate (Fig. 2), and a dolomite peak occurs in the correlative interval in the ACEX record (Vogt, 2009).

In addition to iceberg load, turbid meltwater can also travel to distant locations in suspension plumes or hyperpicnal flows (e.g., Ó Cofaigh et al., 2003). Large volumes of deglacial sediments were likely discharged into the Arctic Ocean with the drainage of proglacial lakes such as reconstructed for both the LIS and EAIS (Mangerud et al., 2004; Klotsko et al., 2019). We assume that some intervals in Units 2 and 5 composed of well-sorted fine grains with a mode at ~2–3 μm (Fig. 5) could be formed from meltwater suspension.

Sedimentary environments for Unit 6 show some features similar to Units 1–4 along with distinct patterns, such as a poorly sorted but overall fine background sediment (Figs. 3, 5). A similar grain-size composition has been shown for glacial intervals lacking massive deposition of coarse IRD in the LR cores (O'Regan et al., 2014). We therefore infer that Unit 6 represents a glacial maximum and low sea level, when the Arctic Ocean possibly had an extensive sea-ice cover with sluggish surface circulation and reduced iceberg discharge. Alternatively, this sediment could be formed from dust blown by katabatic winds from the ice sheets. While the grain size of Unit 6 is overall finer than common for glacial dust, such as Asian loesses (e.g., Prins and Vriend, 2007), its composition depends on the source material and wind speed. For example, glacial dust deposits from the Southern Ocean feature primary modes at 3–4 μm, comparable to Unit 6 (Van der Does et al., 2021).

5.1.3. Sediment redistribution

Debris flows on the slopes and ensuing turbidity currents in the basins provide considerable sediment redistribution in the central Arctic Ocean (e.g., Stein, 2008; Pérez et al., 2020; Joe et al., 2020). In particular, seismic data show that the bottom of the Amundsen Basin is filled with thick turbidite sequences (Backman et al., 2004; Pérez et al., 2020; Weigelt et al., 2020; Boggild and Mosher, 2021), which have also been recognized in sediment cores PS 2176 and 2190 (Fig. 1) (Stein, 2008; Svindland and Vorren, 2002). Most of these sediments have been related to gravity flows during glacial/deglacial times, when ice sheets impacted the shelf margins and submarine ridges (Jakobsson et al., 2001, 2008, 2016; Kristoffersen et al., 2004; Pérez et al., 2020).

Core ICE4 is located at the foot of the LR slope with a considerably shallower depth than the surface of turbidite deposits in the Amundsen Basin at ~4000 m (Pérez et al., 2020; Weigelt et al., 2020; Boggild and Mosher, 2021). Furthermore, the slope in this area bears no evidence of sizeable mass transport deposits (Pérez et al., 2020). This setting, which indicates that accumulation of turbidites at the ICE4 site is unlikely, is consistent with the ICE4 lithostratigraphy lacking apparent gradational sediment cyclicity (Fig. 3, Supplementary Fig. S1). Potential lamination/banding in the lower part of Unit 2 co-occurs with the interval of highest IRD peaks and Ca inputs indicative of iceberg pulses. Distinct, mm- to cm-scale laminations in Unit 7 and Unit 4 are formed by dark laminae related to Mn peaks (Fig. 3). As discussed above, their deposition is likely related to oxidation fronts between sediment pulses. In addition, unlike uniformly silty-clayey sediments of Unit 4, Unit 7 shows interlamination with fine sand (Figs. 3, 5). The sand material could be coming from sediment winnowing and resuspension up-slope from the core site or from pulsed sedimentation following an earlier glacial event.

5.2. Organic matter

Multiple studies demonstrate that OC in Arctic Ocean sediments is mostly terrigenous matter redeposited from surrounding landmasses (Stein and Macdonald, 2004; Goñi et al., 2005; Belicka and Harvey, 2009; Yunker et al., 2009; Martens et al., 2020). This composition results from low primary production in ice-covered waters and a prevalence of physical processes eroding terrestrial OC and transporting it to the Arctic Ocean. The resultant sedimentary OC content is therefore mostly unsuitable for investigating marine biogeochemical processes, but its composition can provide useful information on depositional conditions and sediment provenance (Yamamoto et al., 2008; Yamamoto and Polyak, 2009; Martens et al., 2020). The OC composition is also important for interpreting the $^{14}C_{OC}$ data (Subt et al., 2017; Suzuki et al., 2021).

The TOC content decrease from the core top to ~80 cm depth is consistent with other Arctic Ocean records and can be largely attributed to the diagenetic loss (Stein et al., 2001; Yamamoto and Polyak, 2009). This relatively deep level of the low background TOC content attainment in ICE4 might result from elevated sedimentation rates. A detrended TOC curve provides a more distinct picture for the upper part of the core and displays an increase around 60 cm (Fig. 4). A strong rise in TOC occurs in Unit 5 along with coarse IRD, likely related to high terrigenous input. Pulses of terrigenous OC have been reported for glacial/deglacial intervals in the Arctic Ocean cores including the LR (Yamamoto et al., 2008; Martens et al., 2020).

Investigation of TOC and biomarker characteristics provides further insights into organic matter origin and sources. A combination of the OC/N ratio and $\delta^{13}C_{org}$ gives clues to identifying marine vs. terrestrial OC origin (Fig. 4). A general co-variation of OC/N with TOC values, except for the uppermost part of the core (to the middle of Unit 2), corroborates the terrestrial OC prevalence. Most of the $\delta^{13}C_{org}$ data, including all samples in Units 1–4, range within −22 to −24 ‰. These numbers are similar to those in core 31PC located closer to the Eurasian margin (Fig. 1), where $\delta^{13}C_{org}$ ratios heavier than ~ − 23.5 ‰ were identified as a marine signature (Martens et al., 2020). However, this threshold may be higher in the central Arctic Ocean, where very low primary production is supported almost entirely by ice algae with $\delta^{13}C_{org}$ as heavy as −15 to −8 ‰ (Stein and Macdonald, 2004). We infer therefore that sediments in Units 1–3 that have $\delta^{13}C_{org}$ ratios mostly between −22 and − 22.5 ‰ may have some amount of marine OC. A dual-isotope approach using coupled $\delta^{13}C$ and $\Delta^{14}C$ data could potentially provide a more definitive OC source apportionment (e.g., Martens et al., 2019, 2020). However, the unbiased application of this approach requires estimation of pre-depositional ^{14}C activity, which is not feasible in the absence of independent age controls,

Intervals with lighter $\delta^{13}C_{org}$ likely represent increased input of terrestrial components, notably at the OC peak in the upper part of Unit 2 (Fig. 4). This interpretation is consistent with elevated values of long-chain *n*-alkanes (C_{27}-C_{31}) as well as branched GDGT and BIT indicating high plants and soil bacteria as major OC sources (e.g., Meyers and Takemura, 1997; Hopmans et al., 2004; Weijers et al., 2006). The high content of the C_{31} *n*-alkane is potentially indicative of non-woody plants (grasses and shrubs) (Zech et al., 2009), which are prevalent in the high-Arctic environments. The maturation indices (CPI and ACL) confirm a relatively fresh, non-petrogenic OC input at these intervals (Bray and Evans, 1961; Eglinton and Eglinton, 2008). These OC characteristics indicate that the peak in the upper Unit 2, and possibly a smaller one in Unit 1, is comparable to pulses of terrestrial fluxes identified in core 31PC (Martens et al., 2020) and other OC records along the Siberian to Alaskan margin (Tesi et al., 2016; Keskitalo et al., 2017; Martens et al., 2019). These pulses were attributed to melting events of the Late Pleistocene permafrost and release of large amounts of well-preserved OC from ice complex deposits (ICD). Overall, we conclude that OC in Units 1–4 is likely derived from a mixture of redeposited tundra vegetation and soils with local marine production.

In comparison with the upper part of ICE4, OC composition in Units 5–7 has considerably different characteristics and more variability (Fig. 4). Except for two ACL data points near the top of Unit 5, both ACL and CPI indices show predominantly low values indicative of mature, lithogenic OC (Bray and Evans, 1961; Eglinton and Eglinton, 2008). Reworked lithogenic OC is characteristic of intervals related to iceberg transport in records from the North Atlantic (Villanueva et al., 1997) and glacigenic inputs in the Arctic Ocean including the LR (Yamamoto et al., 2004; Winkelmann et al., 2008; Yamamoto and Polyak, 2009; Kremer et al., 2018). Both OC/N and $\delta^{13}C_{org}$ values in Units 5–7 have a very wide spread, reaching values as high as >20 and >−18 ‰, respectively (Fig. 4). High-OC/N and low $\delta^{13}C_{org}$ values consistently indicate terrestrial input for the pronounced OC peak in Unit 5, where abundant coal particles were identified in the >63 mm fraction (Supplementary Table S2). In combination with high maturation (low CPI and ACL values) and long-chain *n*-alkane signature with a balanced C_{27}-C_{31} composition, these characteristics indicate coal as the most likely origin of this OC.

The opposite, apparently marine but lithogenic origin is represented by low OC/N and heavier $\delta^{13}C_{org}$ values combined with high maturation in Unit 6 (Fig. 4). However, the marine origin of these samples is inconsistent with a distinct long-chain *n*-alkane signature predominated by C_{27} indicative of high plants, possibly trees (Zech et al., 2009). Such contradictory OC composition may represent a mixture of different sources. This interpretation is consistent with the inference above that Unit 6 sediment may have been affected by dust from katabatic winds, which could capture material from land- and shelf-based portions of the ice sheet(s).

In addition to high branched GDGT and BIT values co-occurring with elevated TOC content and terrestrial *n*-alkane signature below the Unit 1/2 boundary, branched GDGTs prevail in the lower part of the core (Units 5–7), with an especially high peak in the lower part of Unit 5 (Fig. 4). Considering a strong lithogenic signature of these sediments, we infer that the GDGT composition here primarily indicates soils redeposited together with eroded rocks (Hopmans et al., 2004; Weijers et al., 2006).

Heightened numbers of brassica- and dinosterols occurring in Units 2 and 5 (Fig. 4) might indicate elevated primary production as in some other Arctic records (Birgel and Hass, 2004; Müller et al., 2009). However, their interpretation in ICE4 is not straightforward due to overall low concentrations and a complex pattern of other OC biomarkers at these stratigraphic levels. In Unit 2, peaks of brassica- and dinosterols co-occur with elevated values of terrestrial markers, such as branched GDGT and BIT, which indicates possible redeposition. Especially distinct brassica- and dinosterol peaks in Unit 5 correspond to a fine-grained interval within an overall coarse glacigenic sediment of this unit, and could potentially indicate interstadial conditions with stronger marine inputs at this interval. More research is needed to comprehend this sedimentary environment.

5.3. Age constraints

5.3.1. OC radiocarbon

In most cases, $^{14}C_{OC}$ dating generates ages older than the actual age of deposition due to the presence of old allochthonous carbon (Andrews et al., 1999; O'Regan et al., 2018). The offset can be especially large, up to >10 kyr, in marine depositional systems with high input of terrigenous, commonly old OC, such as in the Arctic and subantarctic (Rosenheim et al., 2008; Suzuki et al., 2021). Furthermore, the offset can vary downcore as the $^{14}C_{OC}$ content in sediment depends on the OC composition and mechanisms of its transport and deposition. Nevertheless, the use of $^{14}C_{OC}$ in carbonate-free sediments is useful at least for constraining the maximal age range (Park et al., 2017; O'Regan et al., 2018).

In some cases, such as in core 31PC (Fig. 1; Martens et al., 2020), $^{14}C_{OC}$ ages are surprisingly close to the ages independently obtained by matching downcore lithostratigraphic variations to the GISP2 paleoclimatic record (Muschitiello et al., 2020). This correspondence is explained by the pre-depositional oxidation and exchange with the atmosphere of the OC derived from the melting permafrost (ICD) and transport by ice and/or surface currents (Martens et al., 2020).

The above interpretation of the OC in ICE4 suggests that the upper part of the core (Units 1–4) mostly contains terrigenous contributions from the Late Pleistocene ICD and fresh tundra vegetation and soil, with some admixture of local marine production (Figs. 3-4). Considering the similarity of these characteristics to those of 31PC, we assume that the old terrestrial OC in ICE4 also experienced some degree of pre-depositional oxidation leading to younger $^{14}C_{OC}$ ages. This inference is corroborated by a mostly similar provenance from the Siberian margin, although the exact sources and transport mechanisms could be somewhat different (e.g., more transport to ICE4 by drifting ice rather than currents). The assumption of the terrigenous OC preconditioning makes sense in view of an overall gradual downcore increase in $^{14}C_{OC}$ ages (Fig. 3). This obviously non-random pattern can be explained by either an increase in the marine OC contribution in younger sediments or a progression in the age of terrestrial OC delivered to the core site. A lack of a comparable trend in the OC parameters (Fig. 4) does not support the interpretation of a gradual increase in the marine OC input, which indicates the likelihood of a similar distribution of $^{14}C_{OC}$ and actual depositional ages. This pattern can be complicated by deposition of unoxidized old OC, such as from icebergs. In particular, a cluster of apparent old age outliers at 70–80 cm around one of the largest IRD peaks (Fig. 3) results in a ~ 10 kyr inversion from the general trend. A

similar inversion in $^{14}C_{OC}$ ages has been found in iceberg deposits of the last glaciation on the Chukchi shelf (Park et al., 2017).

The $^{14}C_{OC}$ distribution in ICE4 can be evaluated through a comparison with the series of ^{14}C ages obtained on biogenic carbonate (foraminiferal tests) in cores from the LR (Fig. 6) (Spielhagen et al., 1997, 2004; Hanslik et al., 2010). All three cores show a consistent downcore increase in ^{14}C ages in sediments overlying the coarse IRD unit associated with the Middle Weichselian glaciation, MIS 4/3. Core 18TC features a distinct hiatus at 28–29 cm corresponding to the LGM, between 26 and 27 and 13–14 cal. ka, depending on the reservoir correction used (Hanslik et al., 2010). The LGM hiatus or near-hiatus attributed to heavy sea ice cover or an ice shelf, has been identified in multiple Arctic records especially in the western Arctic Ocean (Darby et al., 1997; Polyak et al., 2009), including the central LR (Chiu et al., 2017). In core PS2185 from the LR top the hiatus is not evident probably due to sediment mixing by strong bioturbation or currents. Intensified current impact on the LR is consistent with overall much lower sedimentation rates at the ridge top. An increase in current activity during glacial/deglacial events could be potentially related to massive meltwater discharge and tidal pumping at the glacial fronts (Griffiths and Peltier, 2008, 2009).

Despite considerably higher apparent sedimentation rates in ICE4, the LGM hiatus here is not evident either, possibly indicating more persistent sediment deposition across the LGM. We note that a more accurate identification of the LGM is difficult due to the uncertainties with the ^{14}Coc ages further complicated by the inter-laboratory ^{14}C offset as discussed above. Some additional constraints may be provided by relating an OC peak with a distinct terrestrial composition centered at ~50–60 cm (Fig. 4) to a pronounced ICD pulse dated to 28 ka in core 31PC (Martens et al., 2020). However, despite a similar composition, OC fluxes for these events in ICE4 and 31PC could have had different source areas and thus asynchronous deposition. A smaller OC peak with terrestrial characteristics at ~20–30 cm in ICE4 may correspond to the deglacial ICD pulse identified in multiple records along the Siberian margins (Tesi et al., 2016; Keskitalo et al., 2017; Martens et al., 2019, 2020; Meyer et al., 2019). In this case, these stratigraphic markers bracket a potential LGM hiatus or slowdown in sedimentation rates between ~30 and 50 cm.

Further downcore distribution of the $^{14}C_{OC}$ ages in ICE4 can be evaluated against the position of detrital carbonate pulses in Unit 2 expressed in bulk XRF Ca and XRD dolomite (Fig. 3). Correlative increase in detrital carbonate occurs in cores from the LR top (Figs. 2, 6), although part of this interval may be missing due to the LGM hiatus. A distinct Ca peak at ~30 ka in ICE4 is probably correlative to the whitish dolomitic layer W3 consistently found in cores from the western Arctic Ocean and constrained by multiple ^{14}C dates to the late MIS3, ~30–35 ka (Adler et al., 2009; Polyak et al., 2009; Wang et al., 2013; Zhang et al., 2019). These ages appear to increase in cores located closer to the LIS margin (Schreck et al., 2018; Zhang et al., 2019), possibly due to the old carbon from deglacial waters associated with the erosion of carbonates, as suggested by Polyak et al. (2009). Glacigenic inputs from the LIS margin starting in the late MIS3 are corroborated by terrestrial data indicating that glacial build-up leading to the LGM started after ~40 ka in the northwestern (Keewatin) LIS sector (Dalton et al., 2019). Continuing LIS input in the upper part of ICE4 Unit 2/Unit 1 encompassed by $^{14}C_{OC}$ ages of ~15–30 ka likely corresponds to the LGM and deglaciation, while the Holocene appears to be largely missing (Fig. 3).

While $^{14}C_{OC}$ samples in Units 3–4 are more scarce, they clearly relate this interval to MIS3, with ages roughly between ca. 30 and 40 ka (Figs. 3, 6). Middle MIS3 conditions provide a reasonable background for Unit 3 characterized by the absence of coarse IRD, somewhat elevated, even level of Mn, and elevated content of chlorite relative to illite (Fig. 3). The latter may indicate an open Bering Strait (Yamamoto et al., 2017), which was not impossible in the middle MIS3 (around 40–45 ka), when the global sea level may have risen to ~ − 40 m (Pico et al., 2016). The lowermost pair of $^{14}C_{OC}$ ages of ~35 ka at the bottom of Unit 4 is somewhat younger than expected from the overall age-depth distribution (Figs. 3, 6).

5.3.2. *Paleomagnetic record*

Liu et al. (2019) interpret a 90-cm thick zone of negative inclination in ICE4 (204–115 cm; Figs. 2, 6, 7) as the Matuyama Chron, bounded by geomagnetic reversals at 2.58 and 0.78 Ma. To account for the absence of the Reunion, Olduvai, Cobb Mountain, and Jaramillo normal polarity sub-chrons, Liu et al. (2019) invoked a very low sedimentation rate,

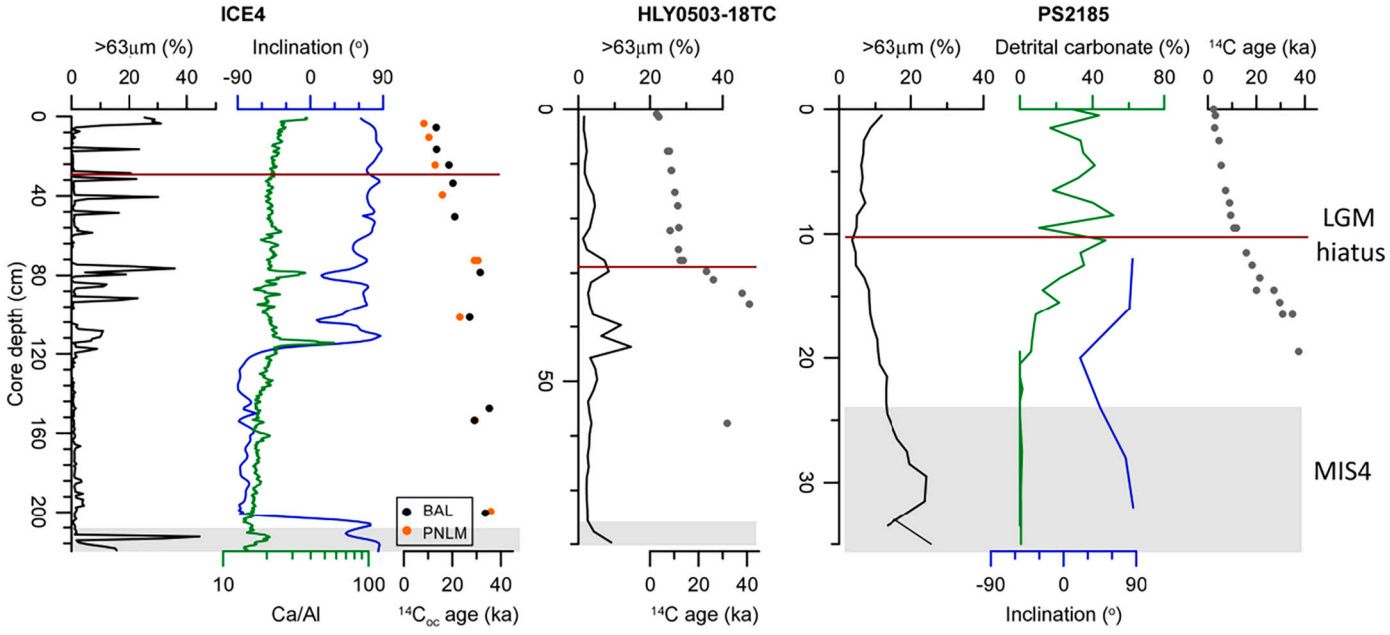

Fig. 6. Stratigraphic correlation of the upper parts of core ICE4, HLY0503-18TC, and PS2185 characterized by multiple ^{14}C ages (Fig. 1; Hanslik et al., 2010; Spielhagen et al., 1997 Svendsen et al., 2004). Other proxies include coarse sediment content (>63 μm), paleomagnetic inclination, and detrital carbonate proxies (XRF Ca/Al for ICE4, detrital carbonate grains for PS2185). See Fig. 2 for a longer stratigraphic context. Distinct glacigenic unit corresponding to MIS 4/3 is highlighted. Horizontal line marks the LGM hiatus apparent in HLY0503-18TC and its correlated position in ICE4 and PS2185.

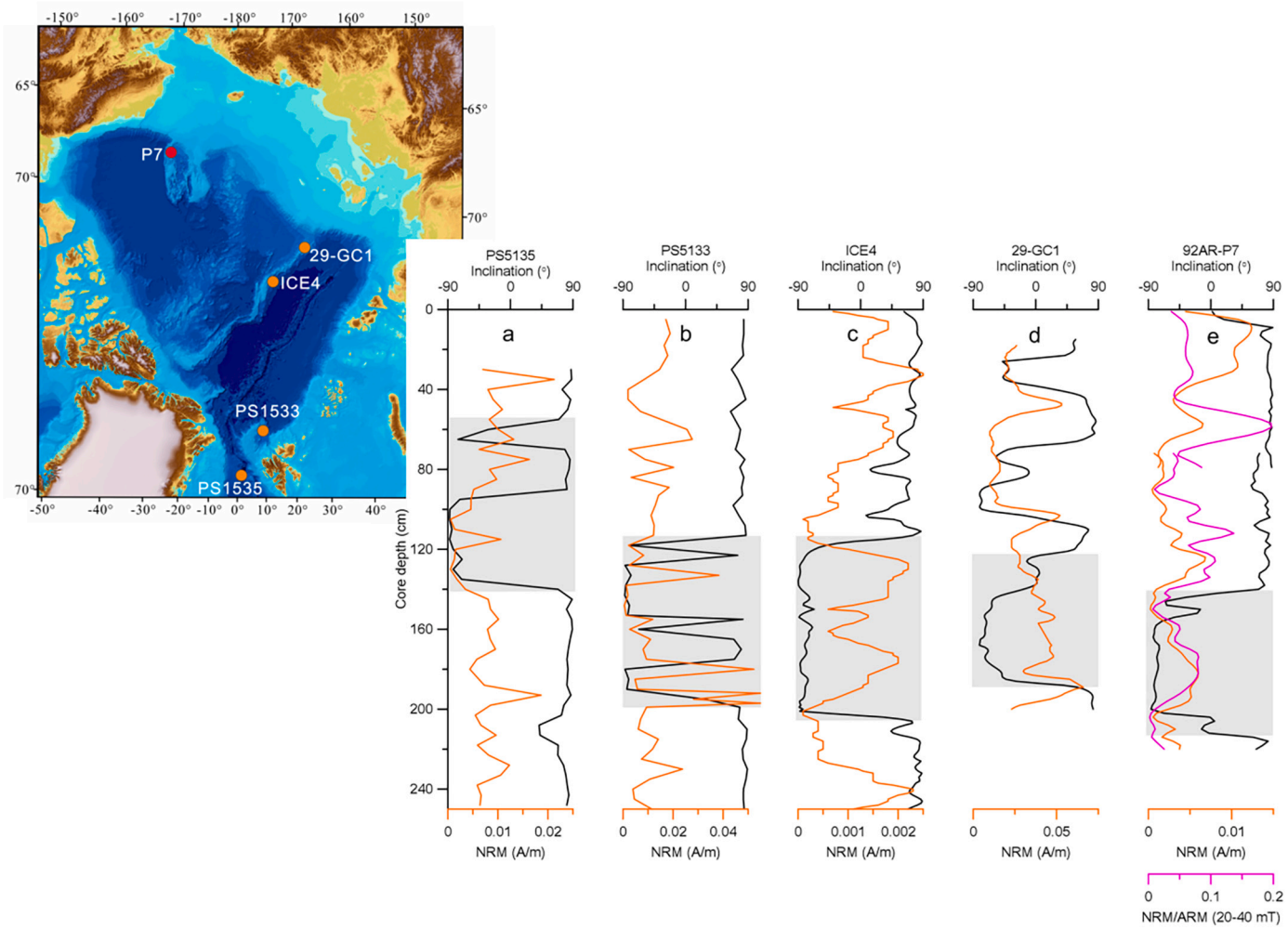

Fig. 7. Comparison of the Arctic Ocean paleomagnetic records of the last ~50 ka with the pronounced MIS 3 negative inclination interval (highlighted) ((a-e): Nowaczyk and Baumann, 1992; Nowaczyk et al., 1994; Liu et al., 2019; West et al., 2021; and this study). See also Polyak et al. (2007) for core 92AR-P7 (P7) stratigraphy. All data sets show the ChRM inclination (black) and NRM intensity (orange). Inclination and NRM intensity shown for cores ICE4 and P7 represent the 20 mT AF demagnetization level. Relative Paleointensity (RPI) is shown for core P7 (NRM/ARM averaged using the 20 to 40 mT AF demagnetization levels).

large lock-in depths, post-depositional smoothing of the remanent magnetization, and/or intervals of non-deposition and erosion. This age model results in sedimentation rates of 0.5–1.5 mm/kyr.

The geomagnetic polarity interpretation of Liu et al. (2019) has several inconsistencies. The Brunhes-Matuyma reversal (0.78 Ma) in both northern and southern hemisphere records falls within interglacial MIS 19 (e.g. Channell et al., 2016; Reilly et al., 2021). Conversely, in ICE4, the inclination transition at 115 cm is above the base of an IRD-rich Unit 2, indicating a glacial environment. Based on North Atlantic data, the Gauss-Matuyama reversal (2.58 Ma) falls within glacial MIS 104 (Channell et al., 2016). In comparison, the ICE4 inclination transition at 204 cm occurs near the bottom of a well-sorted, fine-grained interval indicative of an interglacial-type deposition. If the large lock-in depth hypothesis of Liu et al. (2019) is accepted, then both reversals have been displaced substantially *downward* from their true positions (Roberts and Winklhofer, 2004), and thus should be even more firmly ensconced within the "wrong" stage. Furthermore, the hypothesis of a large lock-in depth requires a thick zone of bioturbation, which is not observed in the ICE4 negative polarity zone and is generally weak in the central Arctic Ocean due to low biological production (Löwemark et al., 2012).

The short-duration Reunion and Cobb Mountain events within the Matuyama chron would not be preserved at very low sedimentation rates of 0.5–1.5 mm/kyr assumed by Liu et al. (2019). However, the Olduvai sub-chron with a ~ 180-kyr duration should form a 9–27-cm thick horizon that should be captured both in the u-channel data generated with a 5-cm resolution magnetometer and in the discrete samples at the ~2-cm sampling interval reported by Liu et al. (2019). In addition, the negative polarity zone in ICE4 has no visually apparent erosional surfaces needed to explain the removal of this interval.

An alternative interpretation for the zone of negative inclination in ICE4 is an expanded record of a geomagnetic excursion within the Bruhnes chron, provided sedimentation rates were sufficiently high. Considering the age framework based on the $^{14}C_{OC}$ data discussed above, this zone may represent a geomagnetic excursion in MIS3 such as the Laschamp Event at 41–42 ka (e.g., Cooper et al., 2021) or a younger Mono Lake Event. The latter "event" may have been a series of geomagnetic fluctuations spanning 30–36 ka (Korte et al., 2019). If the zone of negative inclination in ICE4 represents a merger of the Mono Lake and the Laschamp events, it may have an age of ~30–42 ka, generally consistent with the $^{14}C_{OC}$ age constraints and the interglacial/interstadial lithology of the encompassing sedimentary sediment. This timing yields a sedimentation rate of ~7.5 cm/kyr for the negative inclination zone.

Lithology and redox conditions also affect paleomagnetic records via diagenetic overprints, as demonstrated by several Arctic Ocean studies (Channell and Xuan, 2009; Xuan and Channell, 2010; Xuan et al., 2012). These studies present evidence for the formation of oxidation rims on

titanomagnetite grains, resulting in oxidative titanomaghemite coatings on titanomagnetite grains that carry a self-reversed CRM. Liu et al. (2019) conducted transmission electron microscopy and qualitative x-ray microanalysis of six magnetic extracts from ICE4 samples to investigate the potential presence of this phenomenon. These analyses indicated titanium-free or low-Ti spectra with the exception of the sample from 123 to 125 cm, within the zone of negative inclination, which shows a strong Ti peak. High-resolution imaging and quantitative analysis on a flat, polished specimen is needed to determine if these grains have titanomaghemite rims of the appropriate composition to carry a self-reversed magnetization.

Manganese cycling may contribute to complex diagenetic processes that affect iron oxides, including partial or full removal of titanomaghemite coatings believed to carry self-reversed magnetization (Wiers et al., 2019, 2020). The negative inclination intervals in cores from the Yermak Plateau, including core PS5133 (Figs. 1, 7), and core 29-GC1 from the LR Siberian end were interpreted as post-depositional diagenesis related to Mn cycling (Wiers et al., 2019; West et al., 2022). The ICE4 negative inclination feature may have a similar origin. This zone occurs within fine-grained, mostly hemipelagic interstadial sediment with relatively elevated Mn content, bound by glacigenic deposits above and below this interval. The close correspondence of the inclination transitions with lithologic units suggests this feature may have a diagenetic origin and represent a secondary CRM. Due to these complications affecting the paleomagnetic signal, zones of negative inclination in the Arctic Ocean records should not be used for a direct age control without an accompanying investigation of sediment stratigraphy and geochemical properties as well as consideration of the paleoclimatic environments.

Our multiproxy dataset and age controls for ICE4 allow for this type of a holistic stratigraphic and depositional interpretation. Litho- and chronostratigraphic correlation of ICE4 with the LR core PS2185 (Figs. 2, 6) demonstrates stratigraphic discrepancies of the inclination-based age model of Liu et al. (2019). The negative inclination zone in ICE4 corresponds to an interglacial-type sediment between the last two glaciations, MIS 2 and 4. A diminutive expression of this zone in the correlative interval in PS2185 can be explained by much lower sedimentation rates on the ridge top. Instead, in the absence of litho/chronostratigraphic data, Liu et al. (2019) correlated the ICE4 negative inclination zone to a similar looking feature in PS2185 at a much lower stratigraphic interval below 350 cm (Fig. 2). However, this interval is still considerably younger than the Matuyama Chron as indicated by the age framework for PS2185 and other cores from the LR top (Spielhagen et al., 2004; O'Regan et al., 2008), even considering a recent revision to this stratigraphy based on updated coccolith data (Vermassen et al., 2021).

Negative inclination intervals up to 65 cm thick have been identified in several Arctic Ocean paleomagnetic records with a cm-scale age resolution (Fig. 7) (Nowaczyk and Baumann, 1992; Nowaczyk et al., 1994, 2001; Nowaczyk and Knies, 2000; West et al., 2022). The stratigraphic position of these features constrained to MIS3 is correlative to the negative inclination zone in ICE4. In core P7 from the Northwind Ridge reported here (Fig. 7) the corresponding feature is also confined to the fine-grained, non-glacial sedimentary interval related to MIS3 (Polyak et al., 2007). The occurrence of this negative inclination zone across the Arctic Ocean in cores with relatively elevated sedimentation rates indicates its Arctic-wide nature, although the causes of this event require more investigation. Overall, considering ICE4 sedimentology and independent age constraints, the most internally consistent explanation for the negative inclination zone appears to be either a merger of the Mono Lake and Laschamp geomagnetic excursions or a diagenetic overprint, or possibly a combination of both. Additional insight could be obtained from the construction of a relative paleointensity (RPI) record, which is not presented in Liu et al. (2019). Arctic RPI records are being increasingly used for regional and global Late Quaternary correlations (Caricchi et al., 2019; Scheidt et al., 2022). Anhysteretic remanent magnetization (ARM) measurements from ICE4 are needed to normalize the NRM data for this purpose, as shown in Fig. 7 for core P7.

5.3.3. *Longer stratigraphy*

Below the ICE4 stratigraphy reasonably constrained by ^{14}C ages and the re-interpreted paleomagnetic record, we rely on a cyclo/climatostratigraphic approach and correlation to earlier developed stratigraphies (e.g., Fig. 2). The most conspicuous lithostratigraphic marker is a massive, coarse IRD unit identified in all LR cores (Unit 5 in ICE4). This is the youngest explicit IRD unit in a series of similar stratigraphic features related to glacial/stadial intervals from MIS6 to 4 (Jakobsson et al., 2000, 2001; Spielhagen et al., 2004; O'Regan et al., 2008; Jakobsson et al., 2014; Hanslik et al., 2010). Correlative and older IRD layers are found in cores from other areas of the Arctic Ocean such as the Mendeleev and Alpha ridges and the Makarov, Chukchi, and Canada basins (Polyak et al., 2009; Stein et al., 2010; Wang et al., 2013, 2018; Dong et al., 2017; Xiao et al., 2020, 2021).

Within the general, MIS-scale stratigraphic framework developed for Arctic Ocean records, the age of the specific intervals is difficult to constrain more accurately. Massive IRD layers likely correspond to major deglaciations or ice-sheet instability events, which occur typically at the end of glaciations or stadials (Stokes et al., 2005; Darby and Zimmerman, 2008). In the absence of accurate chronostratigraphic tools for Arctic Ocean sediments, more reliable age constraints come from the terrestrial data. The end of the main Middle Weichselian (MIS 3/4) glaciation in Western Siberia (Barents-Kara or Eurasian Ice Sheet, EAIS) has been constrained to ca. 50 ka, with the deglaciation probably lasting several kyr longer (Svendsen et al., 2004; Moller et al., 2011). The beginning of glacial retreat is more tentatively estimated as ~55–60 ka, and was likely diachronous. Accordingly, most of ICE4 Unit 5 and correlative IRD intervals in Arctic Ocean cores was likely deposited in the early MIS3.

Constraining the ages for Units 6–7 is more difficult as we do not have any information on the underlying sediments (Fig. 3). The attribution of Unit 6 is aided by features indicative of a glacial stage with restricted circulation/iceberg discharge and possibly accumulation of glacigenic dust. These conditions make sense for the time of ice-sheet growth and culmination preceding deglacial events, that is for the interval between ca. 65 and 55 ka (Svendsen et al., 2004; Moller et al., 2011). Unit 7 with a considerably higher content of Mn likely corresponds to upper MIS5a. The lower part of Unit 7 has a pronounced lamination formed by sandy and fine-grained, Mn-enriched layers indicative of a pulsed, possibly post-glacial deposition. MIS5a in the Arctic appears to be a complex interstadial including a distinct glacigenic interval in Arctic Ocean cores (Knies and Vogt, 2003; Adler et al., 2009; Polyak et al., 2009; Schreck et al., 2018). In a core from the northern slope of the Barents Sea this interval was attributed to a discharge of a proglacial lake in west Siberia at estimated ca. 77 ka (Knies and Vogt, 2003). Assuming that this event preceded the deposition of Unit 7, we tentatively constrain its bottom age to ca. 75 ka.

The combination of $^{14}C_{OC}$ data with the negative inclination zone and regional paleoclimatic context provides internally coherent ICE4 age framework (Fig. 8). A linear trend with $R^2 = 0.95$ reasonably approximates the majority of $^{14}C_{OC}$ ages and other tie points discussed above. The resulting age model constrains average sedimentation rates to ~6.5 cm/kyr. This relatively high number for an Arctic Ocean record makes sense for the foot of the slope towards the Eurasian Basin that holds vast accumulation of the Late Cenozoic deposits including extensive glacigenic input (Backman et al., 2004; Pérez et al., 2020; Weigelt et al., 2020). Even on the LR top, average Quaternary sedimentation rates exceed 1 cm/kyr as demonstrated by the ACEX data (Backman et al., 2008; O'Regan et al., 2008). We note, however, that sedimentation rates may have been uneven due to variable depositional environments. Intervals with massive iceberg discharge could be deposited more rapidly, while deposition rates during some other periods were possibly lower, such as expected for the LGM hiatus/slowdown.

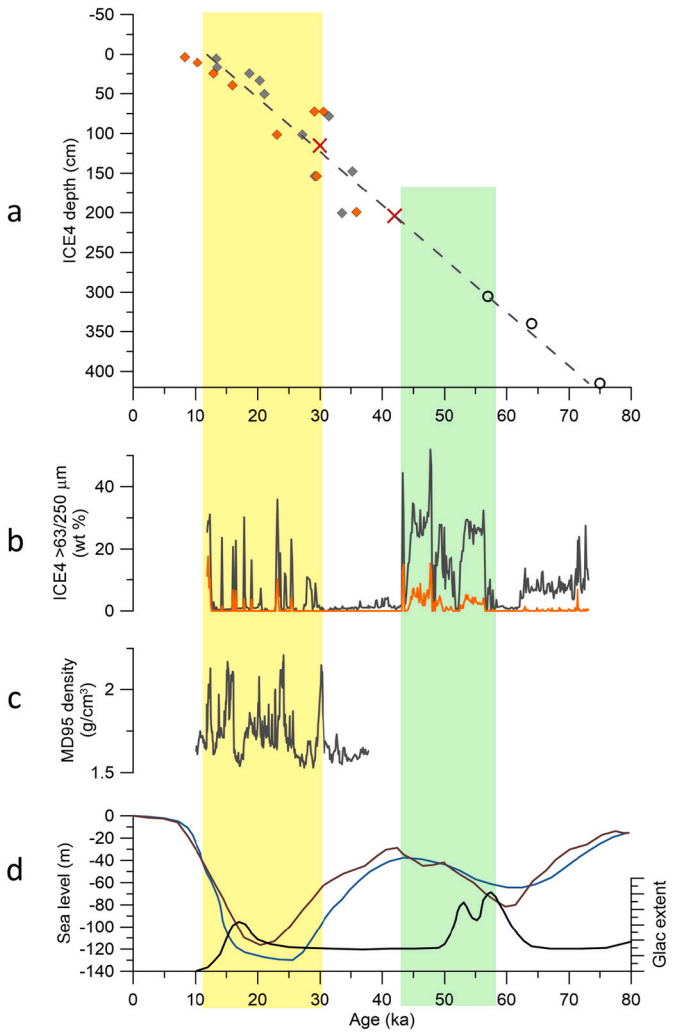

Fig. 8. ICE4 age model and comparison with global and regional glaciation history. (a) ICE4 age-depth plot. Diamonds - $^{14}C_{OC}$ ages (gray - BAL, orange - PNLM); crosses - inclination ties; circles - glaciation ties; dashed line - linear fit. (b) Total (>63-µm, black) and coarse (>250-µm, orange) sand content vs. age. (c) Density in NW Atlantic core MD95–2024 (Weber et al., 2001). (d) Sea level (blue/green lines: Pico et al. (2016), Gowan et al. (2021)) and Siberian glaciation extent (black, relative scale; Svendsen et al., 2004). Marine Isotope Stages (MIS) are shown below. Yellow and green bars - LIS and EAIS glacial inputs. (For interpretation of the references to color in this figure legend, the reader is referred to the web version of this article.)

5.4. *Implications for the history of glacial inputs and circulation*

The developed age constraints enable the interpretation of the ICE4 and correlative Arctic Ocean records in a broad paleoclimatic context. While the available dating approaches are insufficient for a detailed age control, they provide a coherent age model on the MIS scale that accounts for the Late Pleistocene glacial-interglacial history of the Arctic Ocean reconstructed from multiple marine and terrestrial records (e.g., Spielhagen et al., 2004; Svendsen et al., 2004). The time interval under study features high climatic variability including large Middle and Late Weichselian/Wisconsinian glaciations related to sea-level lowstands during MIS 2 and 4, respectively (Fig. 8) (Batchelor et al., 2019; Gowan et al., 2021). The LGM is relatively well constrained by terrestrial data and modeling studies, especially in the North America (Margold et al., 2018; Gowan et al., 2021), but the Middle Weichselian glaciation is much less understood. Nevertheless, this period featured a voluminous ice sheet in Northern Eurasia, only coarsely constrained by chronostratigraphic data (Svendsen et al., 2004; Larsen et al., 2006; Moller et al., 2011). This ice sheet, similar to its smaller LGM counterpart, contained an expansive marine-based component (known as the Barents-Kara Ice Sheet) accounting for almost half of the glaciated area. Furthermore, seafloor data indicate a correlative glaciation in eastern Siberia (East Siberian Ice Sheet, ESIS), which may have been primarily marine-based (Jang et al., 2013; Niessen et al., 2013; Joe et al., 2020). As both age and spatial constraints for this ice sheet are very tentative, its relationship with the EAIS is not well understood.

Stratigraphic distribution of the ICE4 glacial input proxies such as the coarse IRD can be compared with recent models of global sea level (Fig. 8). The proposed age of the IRD unit corresponds to the sea level rise from the MIS 4 minimum to −50-40 m in MIS 3 around ~45 ka (Fig. 9). If the shelf edge at that time was not strongly affected by glacioisostasy, this depth was a likely threshold for flooding much of the Siberian shelves (Jakobsson, 2002), and thus for an extensive detachment of the marine-based ice masses from the ground and destabilization of the entire ice-sheet system. Another factor could be the opening of the Bering Strait with the sill depth ~ 50 m. An open Bering Strait enhances the inflow of the North Atlantic water and thus heat content in the Arctic Ocean (Hu et al., 2015), which is likely to speed up the melting of marine-based ice sheets (e.g., Depoorter et al., 2013).

Similar to the LR cores (e.g., Fig. 2), coarse IRD deposits of Unit 5 contain two thin fine-grained intervals around ca. 50 ka. In core PS2185 a similar interval at ~60 cm depth features a small peak in beryllium isotope ^{10}Be indicating interstadial environments with reduced ice cover and/or increased bioproduction (Spielhagen et al., 2004). A comparable environment can be inferred for this interval in ICE4 from a peak in brassica- and dinosterols (Fig. 4). Overall, this pattern suggests that glacigenic IRD-rich sediments of Unit 5 were deposited in pulses, similar to a stepwise deglaciation in west Siberia (Svendsen et al., 2004).

In contrast to the Middle Weichselian glaciation, the LGM is not expressed in ICE4 in a distinct glacial unit with massive IRD deposition. Instead, it features discrete IRD peaks in Units 1 and 2 constrained to the time interval from the latest MIS 3 to early MIS 1, ca. 30 to 10–15 ka (Fig. 8). This timing is consistent with the terrestrial records of the LGM, especially from North America (e.g., Clark et al., 2009; Gowan et al., 2021). A relatively regular occurrence of Unit 1–2 IRD peaks resembles millennial-scale variability in high-resolution North Atlantic records, such as MD95 cores from the Labrador Sea (Fig. 8) (Weber et al., 2001). While correlating individual peaks requires a more detailed age model, the general similarity of iceberg discharge pattern on the Arctic and Atlantic LIS sides makes sense and has been inferred in several studies (Stokes et al., 2005; Wang et al., 2021).

While a detailed provenance tracking is beyond the scope of this study, the generated mineralogical data indicate considerable differences between the composition of Middle and Late Weichselian/Wisconsinian glacial intervals, as discussed in Section 5.1.2. Elevated content of bulk Ca along with dolomite in Unit 1 and especially Unit 2 reveals LGM contributions from the LIS as shown in multiple cores from the western Arctic Ocean (Clark et al., 1980; Polyak et al., 2009; Stein et al., 2010; Bazhenova et al., 2017; Schreck et al., 2018). Much lower values of these proxies, along with high quartz content and the clay mineral composition featuring high smectite values in Unit 5 (Figs. 2, 3), indicate a predominance of Eurasian over North American glacial input during the Middle Weichselian. In addition to mineral proxies, OC characteristics can provide further insight. The lithogenic composition of the OC peak in Unit 5 likely indicates a coal-bearing source such as coal deposits of the northern West Siberia (Taymyr Peninsula), while a branched GDGT peak in the lower part of this unit signifies redeposition of soils. More detailed provenance attribution for the complex Unit 5 interval requires a more specialized investigation. It is possible that variable segments of the glaciated Siberian margin served as primary sediment sources during MIS 4 to early MIS 3.

A predominance of a particular glacigenic source may depend on the volume and timing of glacial discharge, transportation mechanisms, and circulation patterns. The mostly Eurasian/LIS sources in the Middle/

Late Weichselian (Wisconsinian) intervals are consistent with the reconstructed size of these glaciations in the Arctic (Batchelor et al., 2019; Gowan et al., 2021). While the LIS reached its largest extent and volume in the LGM, the EAIS at this time was smaller than in the Middle Weichselian. A less understood ESIS was also likely larger during MIS4/3, with glacigenic seafloor bedforms attributed to the LGM found only on the Chukchi but not the Eastern Siberian margin (Polyak et al., 2007; Joe et al., 2020; Kim et al., 2021).

Reconstruction of circulation required to deliver Eurasian material to the ICE4 site depends on the specific source locations. Considering the high content of smectite in Unit 5, we assume that a large part if not all of this sediment originated from west Siberia (Wahsner et al., 1999; Vogt and Knies, 2009). This inference is consistent with findings of the EAIS-sourced Middle Weichselian deposits in cores from the western Arctic Ocean including the Canada and Makarov basins and the Northwind Ridge (Dong et al., 2020; Wang et al., 2021; Xiao et al., 2021). A strong cyclonic circulation required for the delivery of this material appears very different from the cimatologically observed TPD (Fig. 1). Nevertheless, this pattern is not dissimilar from the extreme TPD expansion under a strong cyclonic circulation related to the negative Arctic Oscillation (AO) mode (Volkov et al., 2020; Wilson et al., 2021). Deposition on the central LR in this case will have west Siberian provenance. If any material in Unit 5 originated also from the ESIS, it would indicate episodes of delivery by TPD in its typical configuration. In comparison, LIS inputs during the LGM align with the extreme positive AO mode characterized by a strong anticyclonic circulation with an expanded BG (Volkov et al., 2020; Wilson et al., 2021) (Fig. 1). This pattern is consistent with the modeled LGM circulation favorable for an enhanced transport of the LIS material across the central Arctic Ocean (Stärz et al., 2012). It has been suggested that the AO-type circulation modes in the past could have been locked for extended periods of time (Yurco et al., 2010; Darby et al., 2012), but this hypothesis yet needs to be tested. Despite the apparent parallels between the modern, AO-controlled and glacial times circulations, they could have had forcings other than the atmospheric conditions, such as meltwater discharge and sea level that affected the existence of the Bering Strait throughflow and the overall dimensions of the Arctic Ocean. In particular, the Middle Weichselian period featured a strong discharge from the EAIS (Mangerud et al., 2004; Svendsen et al., 2004) combined with intermediate sea levels, possibly with a partially open Bering Strait (Pico et al., 2016). In contrast, the LGM in the Arctic Ocean was predominated by the LIS discharge at very low sea levels that cut off shallow continental shelves including the Bering Strait (Tarasov and Peltier, 2006; Jakobsson et al., 2017).

6. Summary and conclusions

Sediment core ARC5-ICE4 (ICE4) collected by the 5th Chinese Arctic Research Expedition is used for investigating the depositional history in the Eurasian (Amundsen) Basin at the Lomonosov Ridge (LR) foot of slope. ICE4 provides an apparently continuous sedimentary record, not disrupted by erosional processes, such as on the ridge top, or massive deposition of mass-transport deposits in the deeper basin. The ICE4 record is comprised of variable lithologies including distinct glacigenic, mostly iceberg rafted deposits. The age model for ICE4 was developed using a combination of $^{14}C_{OC}$, reevaluated paleomagnetic data of Liu et al. (2019), and correlation to earlier developed stratigraphies. The OC composition indicates its mostly terrigenous origin from glacial erosion or thawing permafrost (ice complex deposits). Nevertheless, the $^{14}C_{OC}$ ages make an orderly succession with depth in the upper part of the core, consistent with other age constraints.

Based on the developed age model, the ICE4 record covers the estimated time interval from ca. 10 to 75 ka (lower MIS 1 to upper MIS 5) including major Late and Middle Weichselian/Wisconsinian glaciations. Respective glacigenic sediments were primarily deposited by pulsed iceberg discharge, possibly with contributions from glacial overflow suspension. The Middle Weichselian interval (MIS 4/3) features a distinct coarse-IRD sedimentary unit with Eurasian provenance. More specific sources of this material are yet to be investigated. The Late Weichselian/Wisconsinian glacial inputs are revealed by sharper IRD peaks featuring mineral proxies of the Laurentide Ice Sheet (bulk Ca, dolomite). These peaks appear to have a millennial-scale periodicity similar to LIS iceberg discharge pulses to the North Atlantic. The differences in sediment composition indicate diverging impacts of the two glaciations on the Arctic Ocean, including ice-sheet sizes/geometries and oceanic circulation. The characteristic Middle/Late Weichselian circulation pathways resemble the extreme positive/negative Arctic Oscillation patterns known from recent observations. The forcings for these glacial-times circulations yet need to be comprehended.

Overall, the study results provide a stratigraphically resolved continuous record of depositional conditions in the central Arctic Ocean encompassing the last two major glacial events. The derived sedimentation rates of several cm/kyr (6.5 cm/kyr average) are consistent with estimates from geophysical data from the Amundsen Basin. This age framework provides a much more coherent stratigraphic and paleoclimatic interpretation than the earlier proposed stratigraphy based on the apparent correlation of geomagnetic reversals (Liu et al., 2019). This comparison highlights the importance of the broad depositional and paleoclimatic context for comprehending sediment records from the Arctic Ocean impacted by profound changes related to glacial-interglacial variability. A widespread presence of a pronounced negative inclination zone in MIS3 sediments indicates that the controls on paleomagnetic record in the Arctic Ocean are not fully understood.

Supplementary data to this article can be found online at https://doi.org/10.1016/j.gloplacha.2022.103993.

Declaration of Competing Interest

We declare that we have no conflict of interest.

Data availability

Data will be made available on request.

Acknowledgments

We thank the team of the 5th Chinese Arctic Research Expedition for core collection. This study was jointly supported by the National Natural Science Foundation of China (No. 41876229), the Basic Scientific Fund for National Public Research Institutes of China (2021Q02), the National Natural Science Foundation of China (No.41876070, 42176245, 41876214, 42022047, 42076079) and the Chinese Polar Environment Comprehensive Investigation & Assessment Programs (No. CHINARE 2017-03-02). Support was also provided by the Marine S&T Fund of Shandong Province for Pilot National Laboratory for Marine Science and Technology (Qingdao) (No. 2018SDKJ0104). Paleomagnetic study of core P7 was supported by the US NSF award OPP-0136238 and kind help from Drs. C. Kissel, C. Laj, and Mr. A. Mazaud during SB's visit to LSCE. One ^{14}C data point for core ICE4 was provided by Dr. J. Liu.

References

Adler, R.E., Polyak, L., Ortiz, J.D., Kaufman, D.S., Channell, J.E.T., Xuan, C., Grottoli, A. G., Sellén, E., Crawford, K.A., 2009. Sediment record from the western Arctic Ocean with an improved late Quaternary age resolution: HOTRAX core HLY0503-8JPC, Mendeleev Ridge. Global and Planetary Change 68, 18–29.

Andrews, J.T., 2000. Icebergs and iceberg rafted detritus (IRD) in the North Atlantic Facts and assumptions. Oceanography 13 (3), 100–108.

Andrews, J.T., Domack, E.W., Cunningham, W.L., Leventer, A., Licht, K.J., Jull, A.J.T., DeMaster, D.J., Jennings, A.E., 1999. Problems and possible solutions concerning radiocarbon dating of surface marine sediments, Ross Sea, Antarctica. Quat. Res. 52, 206–216. https://doi.org/10.1006/qres.1999.2047.

Backman, J., Jakobsson, M., Løvlie, R., Polyak, L., Febo, L.A., 2004. Is the Central Arctic Ocean a sediment starved basin? Quat. Sci. Rev. 23, 1435–1454.

Backman, J., Jakobsson, M., Frank, M., Sangiorgi, F., Brinkhuis, H., Stickley, C., O'Regan, M., Løvlie, R., Pälike, H., Spofforth, D., Gattacecca, J., Moran, K., King, J., Heil, C., 2008. Age model and core-seismic integration for the cenozoic arctic coring expedition sediments from the Lomonosov ridge. Paleoceanography 23, A1S03. https://doi.org/10.1029/2007pa001476.

Batchelor, C.L., Margold, M., Krapp, M., Murton, D.K., Dalton, A.S., Gibbard, P., Stokes, C.R., Murton, J.B., Manica, A., 2019. The configuration of Northern Hemisphere ice sheets through the Quaternary. Nat. Commun. 10, 3713. https://doi.org/10.1038/s41467-019-11601-2.

Bazhenova, E., Fagel, N., Stein, R., 2017. North American origin of "pink–white" layers at the Mendeleev Ridge (Arctic Ocean) new insights from lead and neodymium isotope composition of detrital sediment component. Mar. Geol. 386, 44–55.

Belicka, L.L., Harvey, H.R., 2009. The sequestration of terrestrial organic carbon in Arctic Ocean sediments A comparison of methods and implications for regional carbon budgets. Geochim. Cosmochim. Acta 73, 6231–6248. https://doi.org/10.1016/j.gca.2009.07.020.

Belt, S.T., Massé, G., Rowland, S.J., Poulin, M., Michel, C., LeBlanc, B., 2007. A novel chemical fossil of palaeo sea ice IP25. Org. Geochem. 38, 16–27.

Birgel, D., Hass, H.C., 2004. Oceanic and atmospheric variations during the last deglaciation in the Fram Strait (Arctic Ocean): a coupled high-resolution organic-geochemicaland sedimentological study. Quat. Sci. Rev. 23, 29–47.

Biscaye, P.F., 1965. Mineralogy and sedimentation of recent deep-sea clay in the Atlantic Ocean and adjacent seas and oceans. The Geological Society America Bulletin 76, 803–832.

Bischof, J.F., Darby, D.A., 1997. Mid-to late Pleistocene ice drift in the Western Arctic Ocean evidence for a different circulation in the past. Science 277, 74–78.

Björk, G., Jakobsson, M., Rudels, B., Swift, J.H., Anderson, L., Darby, D.A., Backman, J., Coakley, B., Winsor, P., Polyak, L., Edwards, M., 2007. Bathymetry and deep-water exchange across the Central Lomonosov Ridge at 88–89°N. Deep-Sea Res. I Oceanogr.Res. Pap. 54 (8), 1197–1208.

Björk, G., Jakobsson, M., Assmann, K., Andersson, L.G., Nilsson, J., Stranne, C., Mayer, L., 2018. Bathymetry and oceanic flow structure at two deep passages crossing the Lomonosov Ridge. Ocean Sci. 14, 1–13. https://doi.org/10.5194/os-14-1-2018.

Boggild, K., Mosher, D.C., 2021. Turbidity currents at polar latitudes: A case study of NP-28 channel in the Amundsen Basin. Arctic Ocean. Marine Geology 440, 106571.

Bray, E.E., Evans, E.D., 1961. Distribution of n-paraffins as a clue to recognition of source beds. Geochin. Cosmochim. Acta. 22, 2–15.

Caricchi, C., Lucchi, R.G., Sagnotti, L., Macrì, P., Di Roberto, A., Del Carlo, P., Husum, K., Laberg, J.S., Morigi, C., 2019. A high-resolution geomagnetic relative paleointensity record from the Arctic Ocean deep-water gateway deposits during the last 60 kyr. Geochem., Geophys. Geosyst. 20, 2355–2377. https://doi.org/10.1029/2018GC007955.

Channell, J.E.T., Xuan, C., 2009. Self-reversal and apparent magnetic excursions in Arctic sediments. Earth Planet. Sci. Lett. 284, 124–131.

Channell, J.E.T., Hodell, D.A., Curtis, J.H., 2016. Relative paleointensity (RPI) and oxygen isotope stratigraphy at IODP Site U1308 North Atlantic RPI stack for 1.2–2.2 Ma (NARPI-2200) and age of the Olduvai Subchron. Quat. Sci. Rev. 131, 1–19. https://doi.org/10.1016/j.quascirev.2015.10.011.

Chiu, P.-Y., Chao, W.-S., Gyllencreutz, R., Jakobsson, M., Li, H.-C., Loewemark, L., O'Regan, M., 2017. New constraints on Arctic Ocean Mn stratigraphy from radiocarbon dating on planktonic foraminifera. Quat. Int. 447, 13–26.

Clark, D., Hanson, A., 1983. Central Arctic Ocean sediment texture a key to ice transport mechanisms. In: Molnia, B.F. (Ed.), Glacial-Marine Sedimentation. Plenum Press, New York, pp. 301–330.

Clark, D.L., Whitman, R.R., Morgan, K.A., Mackey, S.D., 1980. Stratigraphy and glacialmarine sediments of the Amerasian Basin, Central Arctic Ocean. Geological Society of America Special Paper 181, 57.

Clark, P.U., Dyke, A.S., Shakun, J.D., Carlson, A.E., Clark, J., Wohlfarth, B., Mitrovica, J. X., Hostetler, S.W., McCabe, A.M., 2009. The last Glacial Maximum. Science 325, 710–714.

Cofaigh, Ó., Taylor, J., Dowdeswell, J.A., Pudsey, C.J., 2003. Palaeo-ice streams, trough mouth fans and high-latitude continental slope sedimentation. Boreas 32 (1), 37–55.

Cook, H. E., Johnson, P.D., Matti, J.C., Zemmels, I.: Methods of sample preparation and X- ray diffraction data analysis, X-ray mineralogy laboratory, In: Kaneps AG, ed. Init Repts, DSDP XXVIII, 999 -1007, http://www.deepseadrilling.Org/28/ volume/dsdp28- appendix-IV. Pdf, 1975.

Cooper, A., Turney, C.S.M., Palmer, J., Hogg, A., Mcglone, M., Wilmshurst, J., Lorrey, A. M., Heaton, T.J., Russell, J.M., Mccracken, K., Anet, J.G., Rozanov, E., Friedel, M., Suter, I., Peter, T., Muscheler, R., Adolphi, F., Dosseto, A., Faith, J.T., Fenwick, P., Fogwill, C.J., Hughen, K., Lipson, M., Liu, J., Nowaczyk, N., Rainsley, E., Bronk Ramsey, C., Sebastianelli, P., Souilmi, Y., Stevenson, J., Thomas, Z., Tobler, R., Zech, R., 2021. A global environmental crisis 42,000 years ago. Science. 371, 811–818. https://doi.org/10.1126/science.abb8677.

Dalton, A.S., Finkelstein, S.A., Forman, S.L., Barnett, P.J., Pico, T., Mitrovica, J.X., 2019. Was the Laurentide ice sheet significantly reduced during marine isotope stage 3? Geology. 47, 111–114.

Darby, D.A., Zimmerman, P., 2008. Ice-rafted detritus events in the Arctic during the last glacial interval and the timing of the Innuitian and Laurentide ice sheet calving events. Polar Res. 27, 114–127.

Darby, D.A., Bischof, J.F., Jones, G.A., 1997. Radiocarbon chronology of depositional regimes in the western Arctic Ocean. Deep Sea Research Part II 44 (8), 1745–1757.

Darby, D.A., Ortiz, J., Polyak, L., Lund, S., Jakobsson, M., Woodgate, R.A., 2009. The role of currents and sea ice in both slowly deposited Central Arctic and rapidly deposited Chukchi-Alaskan margin sediments. Glob. Planet. Chang. 68, 58–72.

Darby, D., Ortiz, J., Grosch, C., Lund, S., 2012. 1,500-year cycle in the Arctic Oscillation identified in Holocene Arctic sea-ice drift. Nature Geoscience 5, 897–900.

Depoorter, M.A., Bamber, J.L., Griggs, J.A., Lenaerts, J.T.M., Ligtenberg, S.R.M., van den Broeke, M.R., Moholdt, G., 2013. Calving fluxes and basal melt rates of Antarctic ice shelves. Nature 502 (7469), 89–92. https://doi.org/10.1038/nature12567.

Dong, L., Liu, Y., Shi, X., Polyak, L., Huang, Y., Fang, X., Liu, J., Zou, J., Wang, K., Sun, F., Wang, X., 2017. Sedimentary record from the Canada Basin, Arctic Ocean implications for late to middle Pleistocene glacial history. Clim. Past 13, 511–531.

Dong, L., Polyak, L., Liu, Y., Shi, X., Zhang, J., Huang, Y., 2020. Isotopic fingerprints of ice-rafted debris offer new constraints on Mid to late Quaternary Arctic circulation and glacial history. G-Cubed 21. https://doi.org/10.1029/2020GC009019 e2020GC009019.

Eglinton, T.I., Eglinton, G., 2008. Molecular proxies for paleoclimatology. Earth Planet. Sci. Lett. 275, 1–16.

Fahl, K., Nöthig, E.-M., 2007. Lithogenic and biogenic particle fluxes on the Lomonosov Ridge (Central Arctic Ocean) and their relevance for sediment accumulation: vertical vs. lateral transport. Deep-Sea Research I 54, 1256–1272.

Folk, R.L., Ward, A.W.C., 1957. Brazos River bar; a study in the significance of grain size parameters. J. Sediment. Res. 27, 3–26.

Gasson, E.G.W., DeConto, R.M., Pollard, D., Clark, C.D., 2018. Numerical simulations of a kilometre-thick Arctic ice shelf consistent with ice grounding observations. Nat. Commun. 9, 1510. https://doi.org/10.1038/s41467-018-03707-w.

Goñi, M.A., Yunker, M.B., Macdonald, R.W., Eglinton, T.I., 2005. The supply and preservation of ancient and modern components of organic carbon in the Canadian Beaufort Shelf of the Arctic Ocean. Mar. Chem. 93, 53–73. https://doi.org/10.1016/j.marchem.2004.08.001.

Gowan, E.J., Zhang, X., Khosravi, S., Rovere, A., Stocchi, P., Hughes, A.L.C., Gyllencreutz, R., Mangerud, J., Svendsen, J.-I., Lohmann, G., 2021. A new global ice sheet reconstruction for the past 80000 years. Nat. Commun. 12, 1199. https://doi.org/10.1038/s41467-021-21469-w.

Griffiths, S.D., Peltier, W.R., 2008. Megatides in the Arctic Ocean under glacial conditions. Geophys. Res. Lett. 35 (8), L08605. https://doi.org/10.1029/2008gl033263.

Griffiths, S.D., Peltier, W.R., 2009. Modeling of Polar Ocean Tides at the last Glacial Maximum Amplification, Sensitivity, and Climatological Implications. J. Clim. 22 (11), 2905–2924. https://doi.org/10.1175/2008JCLI2540.1.

Hanslik, D., Jakobsson, M., Backman, J., Björck, S., Sellén, E., O'Regan, M., Fornaciari, E., Skog, G., 2010. Quaternary Arctic Ocean sea ice variations and radiocarbon reservoir age corrections. Quaternary Sci. Rev. 29, 3430–3441.

Hopmans, E.C., Weijers, J.W.H., Schefuß, E., Herfort, L., Sinninghe Damsté, J.S., Schouten, S., 2004. A novel proxy for terrestrial organic matter in sediments normalized on branched and isoprenoid tetraether lipids. Earth Planet. Sci. Lett. 224, 107–116.

Hu, A., Meehl, G.A., Han, W., Otto-Bliestner, B., Abe-Ouchi, A., Rosenbloom, Nan, 2015. Effects of the Bering Strait closure on AMOC and global climate under different background climates. Prog. Oceanogr. 132, 174–196.

Hughes, T.J., Denton, G.H., Grosswald, M.G., 1977. Was there a late-Würm Arctic ice sheet? Nature 266, 596–602.

Huguet, C., Kim, J.H., Sinninghe Damsté, J.S., Schouten, S., 2006. Reconstruction of glacial-interglacial sea surface temperature in the Arabian Sea using organic proxies. Paleoceanography 21, PA3003. https://doi.org/10.1029/2005PA001215.

Jakobsson, M., 2002. Hypsometry and volume of the Arctic Ocean and its constituent seas. Geochem. Geophys. Geosyst. https://doi.org/10.1029/2001GC000302, 31–18.

Jakobsson, M., Løvlie, R., Al-Hanbali, H., Arnold, E., Backman, J., Mörth, M., 2000. Manganese and color cycle in Arctic Ocean sediments constrain Pleistocene chronology. Geology 28, 23–26.

Jakobsson, M., Lovlie, R., Arnold, E.M., Backman, J., Polyak, L., Knutsen, J.-O., Musatov, E., 2001. Pleistocene stratigraphy and paleoenvironmental variation from Lomonosov Ridge sediments, Central Arctic Ocean. Glob. Planet. Chang. 31, 1–22.

Jakobsson, M., Polyak, L., Edwards, M., Kleman, J., Coakley, B., 2008. Glacial geomorphology of the Central Arctic Ocean the Chukchi Borderland and the Lomonosov Ridge. Earth Surf. Process. Landf. 33, 526–545.

Jakobsson, M., Andreassen, K., Bjarnadóttir, L.R., Dove, D., Dowdeswell, J.A., England, J.H., Funder, S., Hogan, K., Ingólfsson, Ó., Jennings, A., Larsen, N.K., Kirchner, N., Landvik, J.Y., Mayer, L., Mikkelsen, N., Möller, P., Niessen, F., Nilsson, J., O'Regan, M., Polyak, L., Nørgaard-Pedersen, N., Stein, R., 2014. Arctic Ocean glacial history. Quat. Sci. Rev. 92, 40–67.

Jakobsson, M., Nilsson, J., Anderson, L., Backman, J., Björk, G., Cronin, T.M., Kirchner, N., Koshurnikov, A., Mayer, L., Noormets, R., O'Regan, M., Stranne, C., Ananiev, R., Macho, N.B., Cherniykh, D., Coxall, H., Eriksson, B., Flodén, T., Gemery, L., Gustafsson, O., Jerram, K., Johansson, C., Khortov, A., Mohammad, R., Semiletov, I., 2016. Evidence for an ice shelf covering the central Arctic Ocean during the penultimate glaciation. Nat. Commun. 2016 https://doi.org/10.1038/ncomms10365.

Jakobsson, M., Pearce, C., Cronin, T.M., Backman, J., Anderson, L.G., Barrientos, N., Björk, G., Coxall, H., de Boer, A., Mayer, L.A., Mörth, C.-M., Nilsson, J., Rattray, J.E., Stranne, C., Semiletov, I., O'Regan, M., 2017. Post-glacial flooding of the Bering Land Bridge dated to 11 cal ka BP based on new geophysical and sediment records. Clim. Past 13, 991–1005. https://doi.org/10.5194/cp-13-991-2017.

Jang, K., Han, Y., Huh, Y., Nam, S.-I., Stein, R., Mackensen, A., Matthiessen, J., 2013. Glacial freshwater discharge events recorded by authigenic neodymium isotopes in sediments from the Mendeleev Ridge, western Arctic Ocean. Earth Planet. Sci. Lett. 369, 148–157.

Joe, Y.J., Polyak, L., Schreck, M., Niessen, F., Yoon, S.H., Kong, G.S., Nam, S.-I., 2020. Late quaternary depositional and glacial history of the arliss plateau off the east siberian margin in the western Arctic Ocean. Quat. Sci. Rev. 228, 106099.

Kaparulina, E., Strand, K., Lunkka, J.P., 2016. Provenance analysis of Central Arctic Ocean sediments Implications for circumArctic ice sheet dynamics and ocean circulation during late Pleistocene. Quaternary Sci. Rev. 147, 210–220.
Keskitalo, K., Tesi, T., Bröder, L., Andersson, A., Pearce, C., Sköld, M., Semiletov, I.P., Dudarev, O.V., Gustafsson, Ö., 2017. Sources and characteristics of terrestrial carbon in Holocene-scale sediments of the East Siberian Sea. Clim. Past 13, 1213–1226. https://doi.org/10.5194/cp-13-1213-2017.
Kim, S., Polyak, L., Joe, Y.J., Niessen, F., Kim, H.J., Choi, Y., Kang, S.-G., Hong, J.K., Nam, S.-I., Jin, Y.K., 2021. Seismostratigraphic and geomorphic evidence for the glacial history of the northwestern Chukchi margin, Arctic Ocean. Journal of Geophysical Research Earth Surface 126. https://doi.org/10.1029/2020JF006030 e2020JF006030.
Klotsko, S., Driscoll, N., Keigwin, L., 2019. Multiple meltwater discharge and ice rafting events recorded in the deglacial sediments along the Beaufort margin, Arctic Ocean. Quat. Sci. Rev. 203, 185–208.
Knies, J., Vogt, C., 2003. Freshwater pulses in the eastern Arctic Ocean during Saalian and early Weichselian ice-sheet collapse. Quat. Res. 60, 243–251.
Korte, M., Brown, M.C., Panovska, S., Wardinski, I., 2019. Robust characteristics of the laschamp and mono lake geomagnetic excursions results from global field models. Frontiers. Earth Sci. 7 https://doi.org/10.3389/feart.2019.00086 art. no. 86.
Kremer, A., Stein, R., Fahl, K., Ji, Z., Yang, Z., Wiers, S., Matthiessen, J., Forwick, M., Löwemark, L., O'Regan, M., Chen, J., 2018. Snowball I. changes in sea ice cover and ice sheet extent at the Yermak Plateau during the last 160 ka-Reconstructions from biomarker records. Quat. Sci. Rev. 182, 93–108.
Kristoffersen, Y., 1990. On the Tectonic Evolution and Paleoceanographic significance of the Fram Strait Gateway. In: Bleil, U., Thiede, J. (Eds.), Geological History of the Polar Oceans Arctic Versus Antarctic. Kluwer Academic Publishers, pp. 63–76.
Kristoffersen, Y., Sorokin, M.Y., Jokat, W., Svendsen, O., 2004. A submarine fan in the Amundsen Basin, Arctic Ocean. Mar. Geol. 204, 317–324.
Krylov, A.A., Stein, R., Ermakova, L.A., 2014. Clay minerals as indicators of late quaternary sedimentation constraints in the Mendeleev rise, Amerasian Basin, Arctic Ocean. Lithol. Mineral Resour. 49, 103–116.
Larsen, E., Kjær, K.H., Demidov, I.N., Funder, S., Grøsfjeld, K., Houmark-Nielsen, M., Jensen, M., Linge, H., Lysså, A., 2006. Late Pleistocene glacial and lake history of northwestern Russia. Boreas 35, 394–424.
Liu, J., Shi, X., Liu, Y., Liu, Q., Liu, Y., Zhang, Q., Ge, S., Li, J., 2019. A thick negative polarity anomaly in a sediment core from the central arctic ocean geomagnetic excursion versus reversal. J. Geophys. Res. Solid Earth 124.
Löwemark, L., O'Regan, M., Hanebuth, T.J.J., Jakobsson, M., 2012. Late Quaternary spatial and temporal variability in Arctic deep-sea bioturbation and its relation to Mn cycles. Palaeogeogr. Palaeoclimatol. Palaeoecol. 365–366, 192–208.
Ma, D., 2013. Report of the Fifth Chinese National Arctic Expedition. Chinese. China Ocean Press, Beijing, pp. 1–255.
Mangerud, J., Jakobsson, M., Alexanderson, H., Astakhov, V., Clarke, G.K.C., Henriksen, M., Hjort, C., Krinner, G., Lunkka, J.-P., Möller, P., Murray, A., Nikolskaya, O., Saarnisto, M., Svendsen, J.I., 2004. Ice-dammed lakes, rerouting of the drainage of Northern Eurasia during the last glaciation. Quat. Sci. Rev. 24, 1313–1332.
Margold, M., Stokes, C.R., Clark, C.D., 2018. Reconciling records of ice streaming and ice margin retreat to produce a palaeogeographic reconstruction of the deglaciation of the Laurentide Ice Sheet. Quat. Sci. Rev. 189, 1–30.
Martens, J., Wild, B., Pearce, C., Tesi, T., Andersson, A., Bröder, L., O'Regan, M., Jakobsson, M., Sköld, M., Gemery, L., 2019. Remobilization of old permafrost carbon to Chukchi Sea sediments during the end of the last deglaciation. Global Biogeochem. Cycles 33, 2–14.
Martens, J., Wild, B., Muschitiello, F., O'Regan, M., Jakobsson, M., Semiletov, I., Dudarev, O.V., Gustafsson, Ö., 2020. Remobilization of dormant carbon from Siberian-Arctic permafrost during three past warming events. Science Advances 6 (42), eabb6546. https://doi.org/10.1126/sciadv.abb6546.
März, C., Stratmann, A., Matthiessen, J., Meinhardt, A., Eckert, S., Schnetger, B., Vogt, C., Stein, R., Brumsack, H., 2011. Manganeserich brown layers in Arctic Ocean sediments composition, formation mechanisms, and diagenetic overprint. Geochim. Cosmochim. Acta 75, 7668–7687.
McManus, J., 1988. Grain size determination and interpretation. In: Tucker, M. (Ed.), Techniques in Sedimentology. Backwell, Oxford, pp. 63–85.
Meyer, V.D., Hefter, J., Köhler, P., Tiedemann, R., Gersonde, R., Wacker, L., Mollenhauer, G., 2019. Permafrost-carbon mobilization in Beringia caused by deglacial meltwater runoff, sea-level rise and warming. Environ. Res. Lett. 14, 085003.
Meyers, P.A., Takemura, K., 1997. Quaternary changes in delivery and accumulation of organic matter in sediments of Lake Biwa, Japan. Journal of Paleolimnology. 18, 211–218.
Minakov, A.N., Podladchikov, Y.Y., 2012. Tectonic subsidence of the Lomonosov Ridge. Geology 40 (2), 99–102. https://doi.org/10.1130/G32445.1.
Moller, P., Hjort, C., Alexanderson, H., Sallaba, F., 2011. Glacial history of the Taymyr Peninsula and the Severnaya Zemlya Archipelago, Arctic Russia. In: Ehlers, J., Gibbard, P.L., Hughes, P.D. (Eds.), Developments in Quaternary Science, Quaternary Glaciations - Extent and Chronology, 15, p. 373e384 (Chapter 28).
Müller, J., Massé, G., Stein, R., Belt, S.T., 2009. Variability of Sea-Ice Conditions in the Fram Strait over the past 30,000 years. Nat. Geosci. 2, 772–776.
Muschitiello, F., O'Regan, M., Martens, J., West, G., Gustafsson, Ö., Jakobsson, M., 2020. A new 30 000-year chronology for rapidly deposited sediments on the Lomonosov Ridge using bulk radiocarbon dating and probabilistic stratigraphic alignment. Geochronology 2, 81–91. https://doi.org/10.5194/gchron-2-81-2020.
Niessen, F., Hong, J.K., Hegewald, A., Matthiessen, J., Stein, R., Kim, H., Jokat, W., Nam, S.-I., 2013. Repeated Pleistocene glaciation of the East Siberian Continental margin. Nat. Geosci. 6, 842–846.
Nørgaard-Pedersen, N., Spielhagen, R.F., Erlenkeuser, H., Grootes, P.M., Heinemeier, J., Knies, J., 2003. Arctic Ocean during the last Glacial Maximum Atlantic and polar domains of surface water mass distribution and ice cover. Paleoceanography 18, 1063. https://doi.org/10.1029/2002pa000781.
Nowaczyk, N.R., Baumann, M., 1992. Combined high-resolution magnetostratigraphy and nannofossil biostratigraphy for late Quaternary Arctic Ocean sediments. Deep-Sea Research. Part I Oceanographic Research Papers 39 (2A), S567–S601.
Nowaczyk, N.R., Knies, J., 2000. Magnetostratigraphic results from the eastern Arctic Ocean AMS 14 C ages and relative palaeointensity data of the Mono Lake and Laschamp geomagnetic reversal excursions. Geophys. J. Int. 140, 185–197. https://doi.org/10.1046/j.1365-246x.2000.00001.x.
Nowaczyk, N.R., Frederichs, T.W., Eisenhauer, A., Gard, G., 1994. Magnetostratigraphy data from late Quaternary sediments from the Yermak Plateau, Arctic Ocean evidence for four geomagnetic polarity events within the last 170 ka of the Brunhes Chron. Geophys. J. Int. 117 (2), 453–471.
Nowaczyk, N.R., Frederichs, T.W., Kassens, H., Nørgaard-Pedersen, N., Spielhagen, R.F., Stein, R., Weiel, D., 2001. Sedimentation rates in the Makarov Basin, Central Arctic Ocean A paleomagnetic and rock magnetic approach. Paleoceanography 16 (4), 368–389.
Nürnberg, D., Wollenburg, I., Dethleff, D., Eicken, H., Kassens, H., Letzig, T., Reimnitz, E., Thiede, J., 1994. Sediments in Arctic Sea ice Implications for entrainment, transport and release. Mar. Geol. 119, 185–214.
O'Regan, M., King, J., Backman, J., Jakobsson, M., Pälike, H., Moran, K., Heil, C., Sakamoto, T., Cronin, T.M., Jordan, R.W., 2008. Constraints on the Pleistocene chronology of sediments from the Lomonosov Ridge. Paleoceanography 23, PA1S19. https://doi.org/10.1029/2007PA001551.
O'Regan, M., Sellen, E., Jakobsson, M., 2014. Middle to late Quaternary grain size variations and sea-ice rafting on the Lomonosov Ridge. Polar Res. 33, 23672.
O'Regan, M., Coxall, H., Hill, P., Hilton, R., Muschitiello, F., Swärd, H., 2018. Early Holocene Sea level in the Canadian Beaufort Sea constrained by radiocarbon dates from a deep borehole in the Mackenzie Trough, Arctic Canada. Boreas 47, 1102–1117.
Park, K., Ohkushi, K.I., Cho, H.G., Khim, B.K., 2017. Lithostratigraphy and paleoceanography in the Chukchi rise of the western Arctic Ocean since the last glacial period. Polar Sci. 11, 42–53. https://doi.org/10.1016/j.polar.2017.01.002.
Peng, X., Zhang, T., Frauenfeld, O.W., Du, R., Jin, H., Mu, C., 2021. A holistic assessment of 1979–2016 global cryospheric extent. Earth's Future 9 (e2020EF001969).
Pérez, L.F., Jakobsson, M., Funck, T., Andresen, K.J., Nielsen, T., O'Regan, M., Mørk, F., 2020. Late Quaternary sedimentary processes in the Central Arctic Ocean inferred from geophysical mapping. Geomorphology. 369, 107309 https://doi.org/10.1016/j.geomorph.2020.107309.
Pfirman, S.L., Colony, R., Nürnberg, D., Eicken, H., Rigor, I., 1997. Reconstructing the origin and trajectory of drifting Arctic Sea ice. J. Geophys. Res. 102 (C6), 12575–12586.
Pico, T., Mitrovica, J.X., Ferrier, K.L., Braun, J., 2016. Global ice volume during MIS 3 inferred from a sea-level analysis of sedimentary core records in the Yellow River Delta. Quat. Sci. Rev. 152, 72–79.
Polyak, L., Forman, S.L., Herlihy, F.A., Ivanov, G., Krinitsky, P., 1997. Late Weichselian deglacial history of the Svyataya (Saint) Anna Trough, northern Kara Sea, Arctic Russia. Mar. Geol. 143, 169–188.
Polyak, L., Edwards, M.H., Coakley, B.J., Jakobsson, M., 2001. Ice shelves in the Pleistocene Arctic Ocean inferred from glaciogenic deep-sea bedforms. Nature 410, 453.
Polyak, L., Darby, D.A., Bischof, J., Jakobsson, M., 2007. Stratigraphic constraints on late Pleistocene glacial erosion and deglaciation of the Chukchi margin, Arctic Ocean. Quaternary Research 67234–245. https://doi.org/10.1016/j.yqres.2006.08.001.
Polyak, L., Bischof, J., Ortiz, J.D., Darby, D.A., Channell, J.E.T., Xuan, C., Kaufman, D.S., Lovlie, R., Schneider, D.A., Eberl, D.D., Adler, R.E., Council, E.A., 2009. Late Quaternary stratigraphy and sedimentation patterns in the western Arctic Ocean. Glob. Planet. Chang. 68, 5–17.
Polyak, L., Alley, R.B., Andrews, J.T., Brigham-Grette, J., Cronin, T.M., Darby, D.A., Dyke, A.S., Fitzpatrick, J.J., Funder, S., Holland, M., Jennings, A.E., Miller, G.H., O'Regan, M., Savelle, J., Serreze, M., St. John, K., White, J.W.C., Wolff, E., 2010. History of sea ice in the Arctic. Quat. Sci. Rev. 29, 1757–1778.
Polyakov, I.V., Rippeth, T.P., Fer, I., Baumann, T.M., Carmack, E.C., Ivanov, V.V., Janout, M., Padman, L., Pnyushkov, A.V., Rember, R., 2020. Intensification of near-surface currents and shear in the Eastern Arctic Ocean. Geophys. Res. Lett. 46 https://doi.org/10.1029/2020GL089469 e2020GL089469.
Prins, M.A., Vriend, M., 2007. Glacial and interglacial eolian dust dispersal patterns across the Chinese Loess Plateau inferred from decomposed loess grain-size records. Geochem. Geophys. Geosyst. 8, Q07Q05. https://doi.org/10.1029/2006GC001563.
Reilly, B.T., Tauxe, L., Brachfeld, S., Raymo, M., Bailey, I., Hemming, S., Weber, M.E., Williams, T., Garcia, M., Guitard, M., Martos, Y.M., Pérez, L.F., Zheng, X.F., Armbrecht, L., Cardillo, F.G., Du, Z.H., Fauth, G., Glueder, A., Gutjahr, M., Hernández-Almeida, I., Hoem, F.S., O'Connell, S., Peck, V., Ronge, T.A., Seki, O., Tripathi, S., Warnock, J., 2021. New magnetostratigraphic insights from iceberg alley on the rhythms of Antarctic climate during the Plio-Pleistocene. Paleoceanography and Paleoclimatology 36. https://doi.org/10.1029/2020PA003994 e2020PA003994.
Rigor, I.G., Wallace, J.M., Colony, R.L., 2002. Response of sea ice to the Arctic Oscillation. J. Clim. 15, 2648–2663.
Roberts, A.P., Winklhofer, M., 2004. Why are geomagnetic excursions not always recorded in sediments? Constraints from postdepositional remanent magnetization

lock-in modelling. Earth Planet. Sci. Lett. 227, 345–359. https://doi.org/10.1016/j.epsl.2004.07.040.
Rosenheim, B.E., Day, M.B., Domack, E., Schrum, H., Benthien, A., Hayes, J.M., 2008. Antarctic sediment chronology by programmed-temperature pyrolysis methodology and data treatment. G-cubed. 9 (4), Q04005. https://doi.org/10.1029/2007GC001816.
Scheidt, S., Lenz, M., Egli, R., Brill, D., Klug, M., Fabian, K., Lenz, M.M., Gromig, R., Rethemeyer, J., Wagner, B., Federov, G., Melles, M., 2022. A 62-ka geomagnetic palaeointensity record from the Taymyr Peninsula, Russian Arctic. Geochronology 4, 87–107. https://doi.org/10.5194/gchron-4-87-2022.
Schoster, F., 2005. Terrigenous sediment supply and paleoenvironment in the Arctic Ocean during the late Quaternary reconstructions from major and trace elements. Reports on Polar and Marine Research. 498, 1–149.
Schouten, S., Forster, A., Panoto, F.E., Damsté, J.S.S., 2007. Towards calibration of the TEX86 palaeothermometer for tropical sea surface temperatures in ancient greenhouse worlds. Org. Geochem. 38, 0–1546. https://doi.org/10.1016/j.orggeochem.2007.05.014.
Schreck, M., Nam, S.-I., Polyak, L., Vogt, C., Kong, G.S., Stein, R., Matthiessen, J., Niessen, F., 2018. Improved Pleistocene sediment stratigraphy and paleoenvironmental implications for the western Arctic Ocean off the east Siberian and Chukchi margins. Arktos. 4.
Slater, T., Lawrence, I.R., Otosaka, I.N., Shepherd, A., Gourmelen, N., Jakob, L., Tepes, P., Gilbert, L., Nienow, P., 2021. Review article Earth's ice imbalance. Cryosphere 15, 233–246. https://doi.org/10.5194/tc-15-233-2021.
Spielhagen, R.F., Bonani, G., Eisenhauer, A., Frank, M., Frederichs, T., Kassens, H., Kubik, P.W., Mangini, A., Nörgaard-Pedersen, N., Nowaczyk, N.R., Schäper, S., Stein, R., Thiede, J., Tiedemann, R., Wahsner, M., 1997. Arctic Ocean evidence for late Quaternary initiation of northern Eurasian ice sheets. Geology 25, 783–786.
Spielhagen, R.F., Baumann, K.H., Erlenkeuser, H., Nowaczyk, N.R., Nørgaard-Pedersen, N., Vogt, C., Weiel, D., 2004. Arctic Ocean deep-sea record of Northern Eurasian ice sheet history. Quaternary Sci. Rev. 23, 1455–1483.
Stärz, M., Gong, X., Stein, R., Darby, D.A., Kauker, F., Lohmann, G., 2012. Glacial shortcut of Arctic Sea-ice transport. Earth Planet. Sci. Lett. 357–358, 257–267.
Steele, M., Morison, J., Ermold, W., Rigor, I., Ortmeyer, M., 2004. Circulation of summer Pacific halocline water in the Arctic Ocean. J. Geophys. Res. 109.
Stein, R., 2008. Arctic Ocean Sediments Processes, Proxies, and Paleoenvironment. Elsevier, Amsterdam, pp. 1–592.
Stein, R., 2019. The Expedition PS115/2 of the Research Vessel POLARSTERN to the Arctic Ocean in 2018, edited. Alfred Wegener Institute for Polar and Marine Research, Bremerhaven. https://doi.org/10.2312/BzPM_0728_2019.
Stein, R., Macdonald, R.W., 2004. The Organic Carbon Cycle in the Arctic Ocean. Springer-Verlag Publishing Company, Berlin-New York (363 pp).
Stein, R., Boucsein, B., Fahl, K., de Oteyza, T.G., Niessen, K.F., 2001. Accumulation of particulate organic carbon at the Eurasian continental margin during late Quaternary times controlling mechanisms and paleoenvironmental significance. Glob. Planet. Chang. 31, 87–104.
Stein, R., Matthiessen, J., Niessen, F., Krylov, A., Nam, S., Bazhenova, E., 2010. Towards a better (litho-) stratigraphy and reconstruction of Quaternary paleoenvironment in the Amerasian Basin (Arctic Ocean). Polarforschung 79 (2), 97–121.
Stein, R., Fahl, K., Müller, J., 2012. Proxy Reconstruction of Cenozoic Arctic Ocean Sea-Ice History– from IRD to IP25. Polarforschung 82 (1), 37–71.
Steinbach, J., Holmstrand, H., Shcherbakova, K., Kosmach, D., Gustafsson, R., 2021. Source apportionment of methane escaping the subsea permafrost system in the outer Eurasian Arctic Shelf. Proceedings National Academy of Sciences 118 (10). https://doi.org/10.1073/pnas.2019672118 e2019672118.
Stokes, C.R., Clark, C.D., Darby, D., Hodgson, D.A., 2005. Late Pleistocene ice export events into the Arctic Ocean from the M'Clure Strait Ice Stream, Canadian Arctic Archipelago. Global and Planetary Change 49, 139–162.
Subt, C., Yoon, H.I., Yoo, K.C., Lee, J.I., Leventer, A., Domack, E.W., Rosenheim, B.E., 2017. Sub-ice shelf sediment geochronology utilizing novel radiocarbon methodology for highly detrital sediments. G-cubed. 18 (4), 1404–1418. https://doi.org/10.1002/2016GC006578.
Sun, X., Liu, S., Li, J., Zhang, H., Zhu, A., Cao, P., Chen, M., Zhao, G., Khokiattiwong, S., Kornkanitnan, N., Shi, X., 2019. Major and trace element compositions of surface sediments from the lower Bengal Fan Implications for provenance discrimination and sedimentary environment. J. Asian Earth Sci. 184, 104000.
Suzuki, K., Yamamoto, M., Rosenheim, B.E., Omori, T., Polyak, L., 2021. New radiocarbon estimation method for carbonate-poor sediments A case study of ramped pyrolysis 14C dating of postglacial deposits from the Alaskan margin. Arctic Ocean. Quaternary Geochronology 66, 101215. https://doi.org/10.1016/j.quageo.2021.101215.
Svendsen, J.I., Alexanderson, H., Astakhov, V.I., Demidov, I., Dowdeswell, J.A., Funder, S., Gataullin, V., Henriksen, M., Hjort, C., Houmark-Nielsen, M., Hubberten, H.W., Ingólfsson, O., Jakobsson, M., Kjær, K.H., Larsen, E., Lokrantz, H., Lunkka, J.P., Lysså, A., Mangerud, J., Matioushkov, A., Murray, A., Möller, P., Niessen, F., Nikolskaya, O., Polyak, L., Saarnisto, M., Siegert, R., Siegert, M.J., Spielhagen Stein, R., 2004. Late Quaternary ice sheet history of Northern Eurasia. Quaternary Science Review 23, 1229–1271.
Svindland, K.T., Vorren, T.O., 2002. Late Cenozoic sedimentary environments in the Amundsen Basin, Arctic Ocean. Marine Geology. 186, 541–555.
Tarasov, L., Peltier, W.R., 2006. A calibrated deglacial drainage chronology for the north American continent evidence of an Arctic trigger for the Younger Dryas. Quat. Sci. Rev. 25, 659–688.
Tepes, P., Gourmelen, N., Nienow, P., Tsamados, M., Shepherd, A., Weissgerber, F., 2021. Changes in elevation and mass of Arctic glaciers and ice caps, 2010–2017. Remote Sens. Environ. 261, 112481.
Tesi, T., Muschitiello, F., Smittenberg, R.H., Jakobsson, M., Vonk, J.E., Hill, P., Andersson, A., Kirchner, N., Noormets, R., Dudarev, O.V., Semiletov, I.P., Gustafsson, Ö., 2016. Massive remobilization of permafrost carbon during post-glacial warming. Nat. Commun. 7, 13653. https://doi.org/10.1038/ncomms13653.
Van der Does, M., Wengler, M., Lamy, F., Martínez-García, A., Jaccard, S.L., Kuhn, G., Lanny, V., Stuut, J.-B.W., Winckler, G., 2021. Opposite dust grain-size patterns in the Pacific and Atlantic sectors of the Southern Ocean during the last 260,000 years. Quat. Sci. Rev. 263, 106978 https://doi.org/10.1016/j.quascirev.2021.106978.
Vermassen, F., O'Regan, M., West, G., Cronin, T.M., Coxall, H.K., 2021. Testing the stratigraphic consistency of Pleistocene microfossil bioevents identified on the Alpha and Lomonosov Ridges, Arctic Ocean. Arct. Antarct. Alp. Res. 53, 309–323.
Villanueva, J., Grimalt, J.O., Cortijo, E., Vidal, L., Labeyrie, L., 1997. A biomarker approach to the organic matter deposited in the North Atlantic during the last climatic cycle. Geochim. Cosmochim. Acta 61, 4633–4646. https://doi.org/10.1016/S0016-7037(97)83123-7.
Viscosi-Shirley, C., Mammone, K., Pisias, N., Dymond, J., 2003. Clay mineralogy and multi-element chemistry of surface sediments on the Siberian-Arctic shelf Implications for sediment provenance and grain size sorting. Cont. Shelf Res. 23, 1175–1200.
Vogt, C., 1997. Regional and temporal variations of mineral assemblages in Arctic Ocean sediments as climatic indicator during glacial/interglacial changes. Report on Polar Marine Research 251, 309.
Vogt, C., 2009. Data report semiquantitative determination of detrital input to ACEX sites based on bulk sample X-ray diffraction data. In: Backman, J., Moran, K., McInroy, D. B., Mayer, L.A. (Eds.), The Expedition 302 scientists. Proceedings Integrated Ocean Drilling Program, 302. https://doi.org/10.2204/iodp.proc.302.203.2009, 12 p.
Vogt, C., Knies, J., 2009. Sediment pathways in the western Barents Sea inferred from clay mineral assemblages in surface sediments. Nor. J. Geol. 89, 41–55.
Volkov, V.A., Mushta, A., Demchev, D., 2020. Sea ice drift in the Arctic. In: Johannessen, O.M., Bobylev, L.P., Shalina, E.V., Sandven, S. (Eds.), Sea Ice in the Arctic Past, Present and Future. Springer International Publishing, pp. 301–313. https://doi.org/10.1007/978-3-030-21301-5_7.
Wahsner, M., Müller, C., Stein, R., Ivanov, G., Levitan, M., Shekekhova, E., Tarasov, G., 1999. Clay-mineral distribution in surface sediments of Eurasian Arctic Ocean and continental margin as indicator for source areas and transport pathways – a synthesis. Boreas 28, 216–233.
Wang, R., Xiao, W., Marz, C., Li, Q., 2013. Late Quaternary paleoenvironmental changes revealed by multi-proxy records from the Chukchi abyssal plain,western Arctic Ocean. Glob. Planet. Chang. 108, 100–118.
Wang, R., Polyak, L., Xiao, W., Wu, L., Zhang, T., Sun, Y., Xu, X., 2018. Late-Middle Quaternary lithostratigraphy and sedimentation patterns on the Alpha Ridge,central Arctic Ocean implications for Arctic climate variability on orbital time scales. Quat. Sci. Rev. 181, 93–108.
Wang, R., Polyak, L., Zhang, W., Yu, X., Ye, L., Dong, L., Liu, Y., Wang, W., Diekmann, B., 2021. Glacial-interglacial sedimentation and paleocirculation at the Northwind Ridge, western Arctic Ocean. Quat. Sci. Rev. 258, 106882.
Weber, M.E., Mayer, L.A., Hillaire-Marcel, C., Bilodeau, G., Rack, F., Hiscott, R.N., Aksu, A.E., 2001. Derivation of d18O from sediment core log data: implications for millennial-scale climate change in the Labrador Sea. Paleoceanography 16, 503–514.
Weigelt, E., Jokat, W., Eisermann, H., 2020. Deposition history and Paleo-current activity on the Southeastern Lomonosov Ridge and its Eurasian Flank based on seismic data. Geochemistry Geophysics Geosystems 21. https://doi.org/10.1029/2020GC009133 e2020GC009133.
Weijers, J.W.H., Schouten, S., Hopmans, E.C., Geenevasen, J.A.J., David, O.R.P., Coleman, J.M., Pancost, R.D., Sinninghe Damsté, J.S., 2006. Membrane lipids of mesophilic anaerobic bacteria thriving in peats have typical archaeal traits. Environ. Microbiol. 8 (648–657) https://doi.org/10.1111/j.1462-2920.2005.00941.x.
West, G., Alexanderson, H., Jakobsson, M., O'Regan, M., 2022. Optically stimulated luminescence dating supports pre-Eemian age for glacial ice on the Lomonosov Ridge off the East Siberian continental shelf. Quat. Sci. Rev. 267, 107082.
Wiers, S., Snowball, I., O'Regan, M., Almqvist, B., 2019. Late Pleistocene chronology of sediments from the Yermak Plateau and uncertainty in dating based on geomagnetic excursions. Geochem. Geophys. Geosyst. 20 (7), 3289–3310. https://doi.org/10.3389/feart.2020.00075.
Wiers, S., Snowball, I., O'Regan, M., Pearce, C., Almqvist, B., 2020. The Arctic Ocean Manganese Cycle, an Overlooked Mechanism in the Anomalous Palaeomagnetic Sedimentary Record. Frontiers. Earth Sci. 8 (art. no. 750).
Wilson, C., Aksenov, Y., Rynders, S., Kelly, S.J., Krumpen, T., Coward, A.C., 2021. Significant variability of structure and predictability of Arctic Ocean surface pathways affects basin-wide connectivity. Commun Earth Environ 2, 164. https://doi.org/10.1038/s43247-021-00237-0.
Winkelmann, D., Schafer, C., Stein, R., Mackensen, A., 2008. Terrigenous events and climate history of the Sophia Basin, Arctic Ocean. G-cubed 9, Q07023. https://doi.org/10.1029/2008GC002038.
Xiao, W., Polyak, L., Wang, R., Löwemark, L., Mei, J., You, D., Wang, W., Wu, L., Jin, X., 2020. Middle to late Pleistocene Arctic paleoceanographic changes based on sedimentary records from Mendeleev Ridge and Makarov Basin. Quat. Sci. Rev. 228, 106105.
Xiao, W., Polyak, L., Wang, R., Not, C., Dong, L., Liu, Y., Ma, T., Zhang, T.A., 2021. A sedimentary record from the Makarov Basin, Arctic Ocean, reveals changing middle to late Pleistocene glaciation patterns. Quat. Sci. Rev. 270, 107176 https://doi.org/10.1016/j.quascirev.2021.107176.
Xuan, C., Channell, J.E.T., 2010. Origin of apparent magnetic excursions in deep-sea sediments from Mendeleev-Alpha Ridge, Arctic Ocean. Geochem. Geophys. Geosyst. 11, Q02003. https://doi.org/10.1029/2009GC002879.

Xuan, C., Channell, J.E.T., Polyak, L., Darby, D.A., 2012. Paleomagnetism of Quaternary sediments from Lomonosov Ridge and Yermak Plateau implications for age models in the Arctic Ocean. Quat. Sci. Rev. 32, 48–63.

Yamamoto, M., Polyak, L., 2009. Changes in terrestrial organic matter input to the Mendeleev Ridge, western Arctic Ocean, during the late Quaternary. Global and Planetary Change. Glob. Planet. Chang. 68, 30–37.

Yamamoto, M., Okino, T., Sugisaki, S., Sakamoto, T., 2008. Late Pleistocene changes in terrestrial biomarkers in sediments from the Central Arctic Ocean. Org. Geochem. 39, 754–763.

Yamamoto, M., Nam, S.-I., Polyak, L., Kobayashi, D., Suzuki, K., Irino, T., Shimada, K., 2017. Holocene dynamics in the Bering Strait inflow to the Arctic and the Beaufort Gyre circulation based on sedimentary records from the Chukchi Sea. Clim. Past 13, 1111–1127. https://doi.org/10.5194/cp-13-1111-2017.

Ye, L., Zhang, W., Wang, R., Yu, X., Jin, L., 2020. Ice events along the East Siberian continental margin during the last two glaciations evidence from clay minerals. Mar. Geol. 428, 106289.

Yunker, M.B., Macdonald, R.W., Snowdon, L.R., 2009. Glacial to post-glacial transformation of organic input pathways in Arctic Ocean basins. Glob. Biogeochem. Cycles 23, GB4016. https://doi.org/10.1029/2009GB003503.

Yurco, L.N., Ortiz, J.D., Polyak, L., Darby, D.A., Crawford, K.A., 2010. Clay mineral cycles identified by diffuse spectral reflectance in Quaternary sediments from the Northwind Ridge implications for glacial–interglacial sedimentation patterns in the Arctic Ocean. Polar Res. 29, 176–197.

Zech, M., Zech, R., Morra's, H., Moretti, L., Glaser, B., Zech, W., 2009. Late Quaternary environmental changes in Misiones, subtropical NE Argentina, deduced from multi-proxy geochemical analyses in a palaeosol-sediment sequence. Quat. Int. 196, 121–136.

Zhang, T., Wang, R., Polyak, L., Xiao, W., 2019. Enhanced deposition of coal fragments at the Chukchi margin, western Arctic Ocean Implications for deglacial drainage history from the Laurentide Ice Sheet. Quat. Sci. Rev. 218, 281–292.

Zhao, M., Mercer, Jennifer L., Eglinton, Geoffrey, Higginson, Matthew J., Huang, Chi-Yue, 2006. Comparative molecular biomarker assessment of phytoplankton paleoproductivity for the last 160 kyr off Cap Blanc, NW Africa. Organic Geochem. 37, 72–97.